Objectivity in quasi-brittle structural failure via adaptive formulation and mesh refinement

G. B. Barbat[1], M. Cervera[1], H. Venghaus[1] and M. Chiumenti[1]

[1] International Center for Numerical Methods in Engineering (CIMNE), Technical University of Catalonia – BarcelonaTECH, Edificio C1, Campus Norte, Jordi Girona 1-3, 08034 Barcelona, Spain

gabriel.barbat@upc.edu, miguel.cervera@upc.edu, henning.venghaus@upc.edu, michele.chiumenti@upc.edu

Abstract

In this work, the combined implementation of *Adaptive Formulation Refinement* (AFR) and *Adaptive Mesh Refinement* (AMR) strategies is proposed for the efficient and mesh objective evaluation of quasi-brittle fracture.

A critical issue when computing localized structural failure is the spurious mesh bias dependence of the crack trajectories and collapse mechanisms that ensues when adopting the standard displacement-based finite element (FE) formulation. This problem is resolved by the introduction of the mixed strain/displacement FE formulation, which allows for local convergence, producing mesh objective results.

On the one hand, the proposed AFR approach allows to adaptively switch between the standard and mixed FE formulations during the numerical simulation depending on the level of accuracy required in different regions of the domain. Within this framework, the more accurate mixed formulation is activated only in the areas where the crack onset and evolution take place, while the standard formulation is adopted for the rest of the structure.

On the other hand, the adopted octree-based AMR strategy allows to adaptively refine only certain areas of the domain, also in function of the level of accuracy required. Using this methodology, it is possible to start the simulation with an initially relatively coarse mesh and adaptively introduce several levels of mesh refinement only in the regions of interest, where cracks appear and propagate. This approach guarantees the necessary mesh resolution to capture the fracture phenomenon accurately while further increasing the computational efficiency of the simulation. The subsequent adaptive coarsening of the FE mesh is also allowed.

Structural failure and fracture propagation are reproduced via a local isotropic damage model. For this reason, a refinement/coarsening criterion defined in function of the equivalent effective stress is conveniently adopted with both AFR and AMR strategies.

To assess the capabilities of the proposed method, a set of numerical simulations including benchmark problems and experiments is included. Results show the mesh objectivity and cost-efficiency of the approach combining AFR and AMR in fracture problems. The proposed model is able to reproduce experimental crack paths, collapse mechanisms and force-displacement curves with accuracy and without spurious mesh bias dependence.

The paper includes a comparative assessment of the performance of the proposed method and the standard FE formulation exclusively, showing the superior performance of the AFR methodology and its mesh objectivity. Convergence of the computed results when introducing different levels of AMR is also verified. Computational efficiency of the AFR and AMR techniques is specifically assessed. The combination of AFR and AMR approaches allows to provide accurate and mesh objective results in quasi-brittle fracture problems with very significant savings in computational cost.

Keywords: Cracking, Structural failure, Mixed Finite Elements, Mesh adaptivity, Adaptive refinement.

1. Introduction

The numerical modelling of quasi-brittle fracture using the finite element method has been intensively studied over the last five decades. The issue of the spurious dependency of the computed crack paths with the FE mesh employed when adopting the standard displacement-based formulation has been reported since the 1980s [1-4]. This has resulted in the adoption of many different alternative techniques to model fracture, both at the continuous and discontinuous levels, trying to overcome this issue. A comparative review of alternative methodologies can be found in references [5, 6].

The spurious mesh dependence that takes place when using the standard FE formulation from solid mechanics is caused by the lack of local convergence of stresses and strains. Depending on the cracking criterion, the trajectory of the fractures is governed by the stress fields present at the tip of the crack. These are inaccurately computed with standard FEs, resulting in unreliable and spuriously mesh biased results. This idea is underlined in references [6-9].

In view of this, in previous works [7, 8, 10-15], the authors have proposed the use of the strain/displacement $\boldsymbol{\varepsilon/u}$ finite element formulation to compute fracture with enhanced accuracy and mesh objectivity. In this FE formulation, the strain field is treated as an additional primary unknown of the problem and is interpolated independently from the displacements, rather than being computed by local differentiation at element level. This allows to improve the order of convergence and the accuracy of the computed strains and stresses. Specifically, it allows to achieve local convergence of the discrete strain and stress fields in the region of the crack tip, this being a critical feature to produce mesh bias objective results.

For the same reason, by introducing the volumetric/deviatoric split into the solid mechanics problem, the 3-field displacement/deviatoric-strain/pressure $\boldsymbol{u/e/}p$ FE formulation has been proposed, showing to produce more accurate and reliable computations with respect to the classical $\boldsymbol{u/}p$ FE in nonlinear problems under incompressible conditions with increased accuracy [16-19].

Therefore, on the one hand, despite the issue of producing spuriously mesh dependent results, the standard FE formulation is used in many applications due to its simplicity and affordable computational cost, which makes it convenient for large-scale analyses. On the other hand, the mixed $\boldsymbol{\varepsilon/u}$ FE formulation has shown to be able of providing numerical results with mesh objectivity and enhanced accuracy, at the expense of treating the strains as additional nodal unknowns on the problem and introducing a relatively larger computational cost in the FE computation.

Notwithstanding, in the specific problem of quasi-brittle fracture, structural failure occurs in the form of a few cracks appearing and evolving in an area representing a reduced part of the whole domain. Both the standard and mixed formulations are compatible and the use of the more accurate mixed formulation is required only in the small part of the total domain where crack propagation occurs while in the rest of the structure the less costly standard formulation may be adopted.

In view of this, in the present work the *Adaptive Formulation Refinement* (AFR) strategy is implemented to adaptively switch between the standard and mixed $\boldsymbol{\varepsilon/u}$ FE formulations in different regions of the domain depending on the required accuracy, so that an efficient computation framework is defined. The use of isotropic damage models to represent the degradation of the material allows to propose a criterion established in terms of the equivalent effective stress to decide on toggling between the standard and mixed formulations. The AFR

methodology was originally proposed in reference [20] for selectively activating the u/p and u/e/p mixed formulations in the simulation of friction stir welding (FSW) processes.

In the present work, the use of the AFR strategy is proposed in conjunction with an *Adaptive Mesh Refinement* (AMR) framework. AMR has been often employed in alternative models for fracture [21-25]. The adopted approach uses an octree-based method [26-29] to further increase the efficiency of the numerical model by adaptively refining only the areas of the domain where crack propagation occurs. This allows to reproduce the phenomenon of fracture with proper FE resolution while maintaining a coarser mesh elsewhere. The method includes the adaptive refinement and coarsening of the FE mesh according to a criterion also defined in terms of the equivalent effective stress.

The objectives of the present work are: (1) to establish the necessary features required in the implementation of the approach for quasi-brittle fracture based on the AFR and AMR strategies, (2) to demonstrate the capabilities of the proposed model in structural failure problems, (3) to show the ability of the model in reproducing experimental results in terms of collapse mechanisms, force-displacement curves and crack trajectories with precision, (4) to verify the capacity of the proposed approach combining the AFR and AMR methodologies to produce mesh objective results, (5) to assess the performance of the method with regard to accuracy and computational efficiency.

The outline of the paper is the following. In Section 2 the mixed strain/displacement $\boldsymbol{\varepsilon/u}$ finite element formulation used to solve the structural problem is introduced, including the strong and weak continuous forms as well as the corresponding discrete FE approximation The isotropic damage constitutive law considered to model cracking is presented as well. Section 3 details the AFR (Section 3.1) and AMR (Section 3.2) methodologies adopted. Section 4 includes the numerical simulations of structural failure performed to assess the capabilities of the proposed model. Section 5 closes the paper with the conclusions of the work.

2. Finite element formulation

Many different methods for the FE computation of quasi-brittle fracture have been proposed in the literature. By far, the most employed one, both by academics and practitioners, is the *crack band model*, which relies on the use of the standard displacement-based FE formulation for continuum solid mechanics (CSM) problems. This approach, proposed by Rashid in 1968 [30], is applied together with a constitutive law featuring softening such as damage or plasticity to represent material failure at local level. In 1983, Bazant and Oh [31] introduced the objective evaluation of the softening behavior of the material with respect to the FE size, allowing to obtain results independent of the FE mesh size when computing fracture with the crack band model.

Regrettably, the trajectories of the cracks computed with the standard displacement-based FE formulation are spuriously dependent on the orientation of the mesh employed for the analysis. This well-known issue since the 1980's [1-4] renders the method useless in practice.

Although not generally recognized, this is caused by the lack of local convergence of stresses and strains of the standard FE formulation [7, 8]. Near the vicinity of the tip of the crack, the stress and strain fields which are locally used to determine the path of the fracture are computed inaccurately, resulting in the spurious mesh bias dependence of the results.

The use of the mixed strain/displacement $\boldsymbol{\varepsilon/u}$ FE formulation for solid mechanics has been proposed by Cervera and coworkers [7, 8, 10-15] as an effective remedy. In this approach, the strains are treated as additional primary unknowns of the problem, together with the

displacements. The mixed formulation has proven to be locally convergent in terms of strains and stresses [7, 8] and, consequently, to produce mesh-bias independent results in cracking problems.

Previous studies analyzing the comparative performance of the standard and mixed $\boldsymbol{\varepsilon/u}$ formulations have extensively shown, on the one hand, the inability of the standard FEs of delivering results without spurious mesh dependence on the FE orientation and, on the other hand, the capacity of the mixed FEs for consistently producing reliable mesh objective computations [13, 15]. Also, it has been demonstrated that convergence of the computed stresses, strains and mechanical dissipation is guaranteed with mixed FEs [18].

Notwithstanding, the mixed $\boldsymbol{\varepsilon/u}$ FE formulation introduces the strain field as an additional primary unknown of the solid mechanics problem being solved, together with the displacements, resulting in a higher cost of the numerical simulations. In the present work the efficiency of the mixed FEM is increased by adaptively activating the mixed formulation only in the regions where local accuracy is required in order to obtain convergent and mesh objective results, while using the standard formulation elsewhere. Computational efficiency of the mixed FEM is further increased in the present work with the adoption of the Adaptive Formulation Refinement approach.

The proposed approach preserves the local format of the problem. Fracture propagation is computed according to the local values of the stress field at the tip of the developing crack, without introducing gradient or higher order terms in the constitutive law or regularizing terms in the variational form. Note that, as it is pointed out in reference [6], crack models regularized at continuous level require the adoption of very fine meshes. This results in an important increase of the computational cost involved in the calculations when compared to the crack band model, much larger than the one ensuing from the use of the mixed $\boldsymbol{\varepsilon/u}$ formulation [6]. For this reason in regularized approaches, such as phase-field models, adaptive mesh refinement capabilities are often adopted [21-25]. The issue of computational cost has also been addressed in reference [32] by computing the nodal phase-field variable only in a predefined reduced sub-domain where cracking occurs rather than in the whole structure. An appraisal of the computational costs involved in the alternative methods proposed for the evaluation of localized structural failure can be found in the comparative study of reference [6].

Continuous formulation

In the rest of this section, the mixed strain/displacement $\boldsymbol{\varepsilon/u}$ FE formulation employed for the mesh objective evaluation of quasi-brittle failure is presented. For additional details the interested reader is referred to references [7, 8, 11, 12, 14, 33-35].

The displacements $\boldsymbol{u}$ and the strains $\boldsymbol{\varepsilon}$ are adopted as primary unknowns of the nonlinear solid mechanics problem. The compatibility equation relates these two fields in the way:

$$\boldsymbol{\varepsilon} = \mathbf{S}\,\boldsymbol{u} \tag{1}$$

$\mathbf{S}$ being the differential symmetric gradient operator.

Also, the Cauchy momentum equation associates the stresses $\boldsymbol{\sigma}$ and the body forces $\mathbf{f}$

$$\mathbf{S}^T\boldsymbol{\sigma} + \mathbf{f} = \mathbf{0} \tag{2}$$

$\mathbf{S}^T$ being the differential divergence operator, adjoint to the $\mathbf{S}$ in Eq. (1).

In addition, the stresses and strains are connected through the constitutive law, established in secant form as

$$\boldsymbol{\sigma} = \mathbf{D}\,\boldsymbol{\varepsilon} \tag{3}$$

where $\mathbf{D} = \mathbf{D}(d)$ is the (nonlinear) secant constitutive matrix, expressed in function of the damage index, d. $\mathbf{D}$ needs to be symmetric and positive semidefinite from thermodynamic considerations.

From the three previous equations, the strong form of the problem is obtained as follows: firstly, Eq. (1) is pre-multiplied by $\mathbf{D}$, and secondly, Eq. (3) is introduced into Eq. (2)

$$-\mathbf{D}\boldsymbol{\varepsilon} + \mathbf{D}\mathbf{S}\boldsymbol{u} = \mathbf{0} \tag{4}$$

$$\boldsymbol{S}^T(\mathbf{D}\boldsymbol{\varepsilon}) + \mathbf{f} = \mathbf{0} \tag{5}$$

Then the corresponding weak form is derived by: (i) multiplying Eqs. (4) and (5) by vectors of virtual strains and virtual displacements respectively, (ii) integrating both equations over the spatial domain and (iii) applying the Divergence Theorem to the first term of Eq. (5). This results in the following system of equations:

$$-\int_\Omega \delta\boldsymbol{\varepsilon}^T\mathbf{D}\boldsymbol{\varepsilon}\,\mathrm{d}\Omega + \int_\Omega \delta\boldsymbol{\varepsilon}^T\mathbf{D}\mathbf{S}\boldsymbol{u}\,\mathrm{d}\Omega = 0 \quad \forall\delta\boldsymbol{\varepsilon} \tag{6}$$

$$\int_\Omega (\mathbf{S}\delta\boldsymbol{u})^T(\mathbf{D}\boldsymbol{\varepsilon})\mathrm{d}\Omega = \int_\Omega \delta\boldsymbol{u}^T\mathbf{f}\,\mathrm{d}\Omega + \int_{\Gamma_t} \delta\boldsymbol{u}^T\bar{\mathbf{t}}\,\mathrm{d}\Gamma \quad \forall\delta\boldsymbol{u} \tag{7}$$

Note that the boundary Γ of the domain is divided in two parts, Γ_u and Γ_t, corresponding to the Dirichlet and Newmann boundary conditions.

The variational form of the problem consists in finding the strain and displacement fields $\boldsymbol{\varepsilon}$ and $\boldsymbol{u}$ complying with the system of Eqs. (6)-(7) and conforming to the boundary condition $\boldsymbol{u} = \mathbf{0}$ in Γ_u given the arbitrary virtual displacement vector $\delta\boldsymbol{u}$, which is also null on Γ_u, and the arbitrary virtual strain vector $\delta\boldsymbol{\varepsilon}$. Note as well that the problem is symmetric.

FE approximation

Once the spatial domain Ω is discretized into nonintersecting finite elements Ω_e, such that $\Omega = \cup\,\Omega_e$, the displacement $\boldsymbol{u}$ and the strain $\boldsymbol{\varepsilon}$ are approximated using independent interpolations $\hat{\boldsymbol{u}}$ and $\hat{\boldsymbol{\varepsilon}}$.

$$\boldsymbol{u} \cong \hat{\boldsymbol{u}} = \boldsymbol{N}_u\boldsymbol{U} \tag{8}$$

$$\boldsymbol{\varepsilon} \cong \hat{\boldsymbol{\varepsilon}} = \boldsymbol{N}_\varepsilon\boldsymbol{E} \tag{9}$$

where $\boldsymbol{U}$ and $\boldsymbol{E}$ are vectors containing the nodal values of the displacements and the strains. $\boldsymbol{N}_u$ and $\boldsymbol{N}_\varepsilon$ are the matrices containing the interpolation functions employed in the FE approximation.

When adopting a mixed FE, the interpolation functions employed needs to fulfill the inf-sup stability condition to avoid spurious oscillations in the computed solution [36-38]. This condition is not satisfied when equal order linear interpolation functions are considered for $\boldsymbol{N}_u$ and $\boldsymbol{N}_\varepsilon$ [37, 39, 40]. In order to use linear interpolation functions for both fields while avoiding spurious oscillations in the computed solution, a stabilization procedure is introduced. The proposed method follows the Variational Multiscale Stabilization approach [41-45].

The procedure is to substitute the strain field approximation in Eq. (9) with the following one

$$\boldsymbol{\varepsilon} \cong \hat{\boldsymbol{\varepsilon}} = \boldsymbol{N}_\varepsilon \boldsymbol{E} + \tau_\varepsilon (\boldsymbol{B}_u \boldsymbol{U} - \boldsymbol{N}_\varepsilon \boldsymbol{E}) = (1 - \tau_\varepsilon) \boldsymbol{N}_\varepsilon \boldsymbol{E} + \tau_\varepsilon \boldsymbol{B}_u \boldsymbol{U} \tag{10}$$

where τ_ε is a stabilization parameter such that $0 \leq \tau_\varepsilon \leq 1$. $\boldsymbol{B}_u$ is the standard compatibility matrix, defined as $\boldsymbol{B}_u = \boldsymbol{S}\boldsymbol{N}_u$. Using $\tau_\varepsilon = 0$ corresponds to adopting the strain interpolation of the non-stabilized mixed problem, while the case $\tau_\varepsilon = 1$ recovers the strain interpolation of the standard displacement-based formulation from solid mechanics.

References [7, 8, 45] have shown that the optimal convergence rate of the problem is attained when considering $\tau_\varepsilon = c_\varepsilon \, h/L$, where $c_\varepsilon = \mathcal{O}(1)$ is an arbitrary constant, L is a reference size of the structure and h is the FE size. In the present work, $c_\varepsilon = 1$ is used. When adaptive mesh refinement is introduced according to the procedure described in the following sections, the FE size h used to compute τ_ε is adjusted accordingly.

Also, taking into consideration the definition of the strain field in Eq. (10), the value of the crack bandwidth b becomes:

$$b = (1 - \tau_\varepsilon) 2h + \tau_\varepsilon h = (2 - \tau_\varepsilon) h \tag{11}$$

By introducing the interpolation function proposed in Eqs. (8) and (10) into the weak form of the problem (6)-(7), the following algebraic system of equations results

$$\begin{bmatrix} -\boldsymbol{M}_{\boldsymbol{\tau}} & \boldsymbol{G}_{\boldsymbol{\tau}} \\ \boldsymbol{G}_{\boldsymbol{\tau}}^T & \boldsymbol{K}_{\boldsymbol{\tau}} \end{bmatrix} \begin{bmatrix} \boldsymbol{E} \\ \boldsymbol{U} \end{bmatrix} = \begin{bmatrix} \boldsymbol{0} \\ \boldsymbol{F} \end{bmatrix} \tag{12}$$

where $[\boldsymbol{E} \quad \boldsymbol{U}]^T$ is the vector containing the nodal values of the unknowns of the problem, strains and displacements, and $\boldsymbol{M}_{\boldsymbol{\tau}} = (1 - \tau_\varepsilon)\boldsymbol{M}$, $\boldsymbol{G}_{\boldsymbol{\tau}} = (1 - \tau_\varepsilon)\boldsymbol{G}$ and $\boldsymbol{K}_{\boldsymbol{\tau}} = \tau_\varepsilon \boldsymbol{K}$. $\boldsymbol{M}$ is a mass-like projection matrix, $\boldsymbol{G}$ is the discrete gradient matrix, $\boldsymbol{K}$ is a stiffness-like matrix and $\boldsymbol{F}$ is the vector of external nodal forces:

$$\boldsymbol{M} = \int_\Omega \boldsymbol{N}_\varepsilon^T \mathbf{D} \boldsymbol{N}_\varepsilon \, \mathrm{d}\Omega \tag{13}$$

$$\boldsymbol{G} = \int_\Omega \boldsymbol{N}_\varepsilon^T \mathbf{D} \boldsymbol{B}_u \, \mathrm{d}\Omega \tag{14}$$

$$\boldsymbol{K} = \int_\Omega \boldsymbol{B}_u^T \mathbf{D} \boldsymbol{B}_u \, \mathrm{d}\Omega \tag{15}$$

$$\boldsymbol{F} = \int_{\boldsymbol{\Omega}} \boldsymbol{N}_u^T \mathbf{f} \, \mathrm{d}\Omega + \int_{\Gamma_t} \boldsymbol{N}_u^T \bar{\boldsymbol{t}} \, \mathrm{d}\Gamma \tag{16}$$

The use of the mixed strain/displacement FE formulation in CSM problems presents the following advantages:

- It does not require any specific FE interpolation and can be used with triangles, quadrilaterals, tetrahedra, hexahedra and prisms [11].
- It does not need any specific development for implementation in 3D [11].
- It can be employed with any suitable constitutive behavior [12, 14, 33].

When used for problems involving quasi-brittle fracture:

- Previous works have shown its applicability with isotropic and orthotropic damage models including crack closure-reopening effects and irreversible straining [12, 14]. Plasticity constitutive laws have also been adopted within this FE formulation [33, 46-48].

- It can accurately reproduce the structural size effect phenomenon [15].
- It can naturally reproduce branching and intersecting cracks without any additional specific developments [6].

Damage constitutive laws

In this work, cracks are modelled using an isotropic continuum damage model, a reformulation of the original crack band model. Alternatively, orthotropic damage models can be adopted [12, 14].

Two versions of the constitutive law are proposed, one featuring the Rankine damage criterion and the other one with the Drucker-Prager damage criterion.

For an isotropic damage model, the constitutive law in Eq. (3) is expressed as

$$\boldsymbol{\sigma} = \mathbf{D}(d)\,\boldsymbol{\varepsilon} = (1-d)\,\mathbf{D}_0\boldsymbol{\varepsilon} \tag{17}$$

where $\mathbf{D} = \mathbf{D}(d)$ is the secant constitutive matrix, written in terms of the internal scalar damage variable d which represents the degradation state of the material. $\mathbf{D}_0$ is the initial elastic constitutive matrix of the undamaged material, which is defined for initially isotropic elastic materials as a function of the initial values of Young's modulus E and Poisson's ratio ν. $\mathbf{D}$ is symmetric and positive semidefinite for $0 \leq d \leq 1$.

The damage criterion $\mathbb{F}$ is introduced as

$$\mathbb{F}\left(\bar{\sigma}_{eq}, r\right) = \bar{\sigma}_{eq}(\overline{\boldsymbol{\sigma}}) - r = 0 \tag{18}$$

where the effective stress $\overline{\boldsymbol{\sigma}}$ is introduced as $\overline{\boldsymbol{\sigma}} = \mathbf{D}_0\,\boldsymbol{\varepsilon}$, following the hypothesis of strain equivalence, the equivalent effective stress $\bar{\sigma}_{eq}$ is defined in function of the damage criterion considered and r is the current damage threshold.

For the Rankine damage criterion, whose surface is plotted in Figure 1a, the equivalent effective stress $\bar{\sigma}_{eq}$ is computed in function of $\overline{\boldsymbol{\sigma}}$ as

$$\bar{\sigma}_{eq}(\overline{\boldsymbol{\sigma}}) = \langle \bar{\sigma}_1 \rangle \tag{19}$$

where $\bar{\sigma}_1$ is the major principal effective stress and $\langle\cdot\rangle$ are the Macaulay brackets, such that $\langle x \rangle = x$ if $x \geq 0$ and $\langle x \rangle = 0$ if $x < 0$.

Alternatively, for the Drucker-Prager damage criterion

$$\bar{\sigma}_{eq}(\overline{\boldsymbol{\sigma}}) = \frac{\sqrt{3J_2} + \alpha I_1}{1+\alpha} \tag{20}$$

where I_1 and J_2 are defined in function of $\overline{\boldsymbol{\sigma}}$ as the first and second effective stress invariants and α is calculated in function of the tensile and compressive strengths of the material f_t and f_c

$$\alpha = \left(\frac{f_c}{f_t} - 1\right) \Big/ \left(\frac{f_c}{f_t} + 1\right)$$

Other damage criteria may be readily used, as shown in references [12, 14].

The initial value of the damage threshold r is the tensile strength of the material f_t. Its current value at time t is determined according to the Kuhn-Tucker optimality and consistency conditions, guaranteeing the positiveness of the dissipation and the irreversibility of damage.

$$r = \max\left(f_t, \max \bar{\sigma}_{eq}(\hat{t})\right) \quad \hat{t} \in [0, t] \tag{21}$$

In the present work considers that the internal damage variable d follows an exponential softening behavior, as shown in Figure 1b:

$$d = 1 - \frac{f_t}{r} \exp\left(-2H_d \frac{\langle r - f_t \rangle}{f_t}\right) \tag{22}$$

where H_d is a softening parameter controlling the rate of degradation of the material.

Alternative softening functions may be used if deemed necessary. They are required to monotonically decrease from 1 to 0 as the damage threshold r evolves from f_t to infinity. Also, the objective definition of the mechanical dissipation needs to be established for each function.

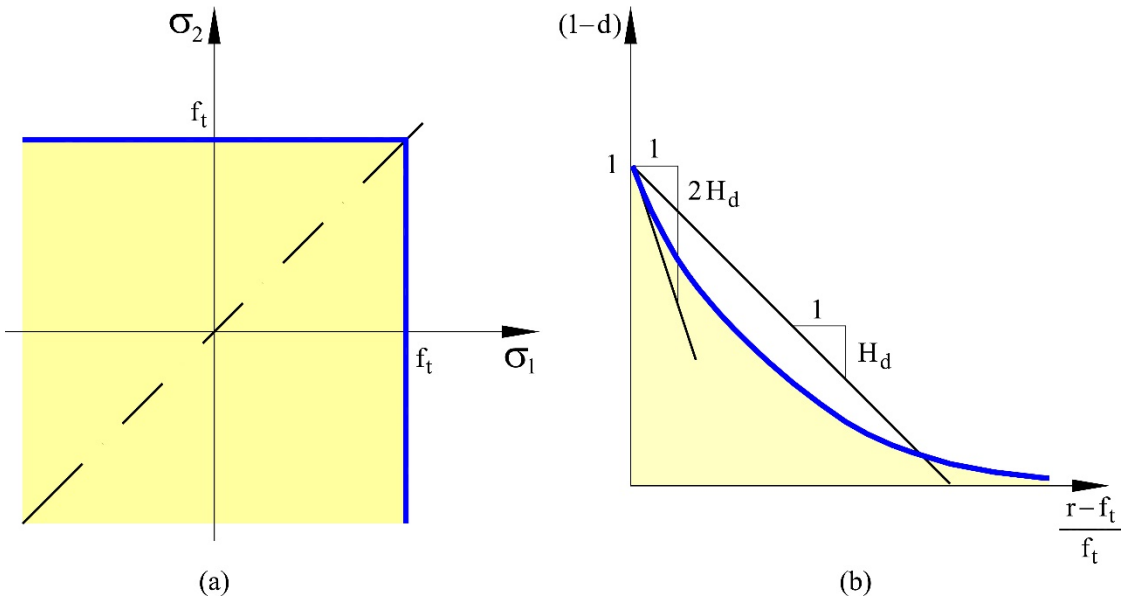

Figure 1. Damage model: (a) Rankine damage surface and (b) softening function

Energy conservation considerations link the softening parameter H_d in Eq. (22) to material properties via Irwin's material length $\mathcal{L} = EG_f/{f_t}^2$ and the crack bandwidth b.

$$H_d = \frac{b}{2\mathcal{L} - b} \tag{23}$$

In this way, the proposed model is able to provide results independent of the crack bandwidth, guaranteeing the objective energy dissipation during the cracking process. The crack bandwidth is computed as in Eq. (11), which yields $b = h$ when using the standard FE formulation ($\tau_\varepsilon = 1$).

3. Adaptivity in quasi-brittle structural failure computations

In this section, the approaches employed for introducing the adaptive mesh refinement (AMR) technique and the adaptive FE formulation refinement (AFR) into the FE computations are presented. They are both implemented with the aim of further increasing the computational efficiency of the proposed mixed $\boldsymbol{\varepsilon/u}$ FE method for computing quasi-brittle fracture while preserving its capacity for producing convergent results with enhanced accuracy and mesh objectivity.

3.1. Adaptive formulation refinement

The present work uses the adaptive application of the standard and mixed strain/displacement FE formulations, as depicted in Figure 2.

References [34, 49] underline the fact that both formulations are compatible. In order to ensure the consistency of the AFR approach in the classical Rayleigh-Ritz sense, the continuity of the interpolated displacement field across element edges needs to be ensured. This requirement is fulfilled when the same interpolation functions are adopted for the displacements for both the standard and mixed formulations. For further details references [34, 49] are recommended.

For this reason, the less costly standard displacement-based formulation may be adaptively switched with the enhanced accuracy mixed formulation only when and where necessary. In the following, the main features of the adopted AFR strategy are presented. For additional details, the original reference [20] introducing the method is recommended.

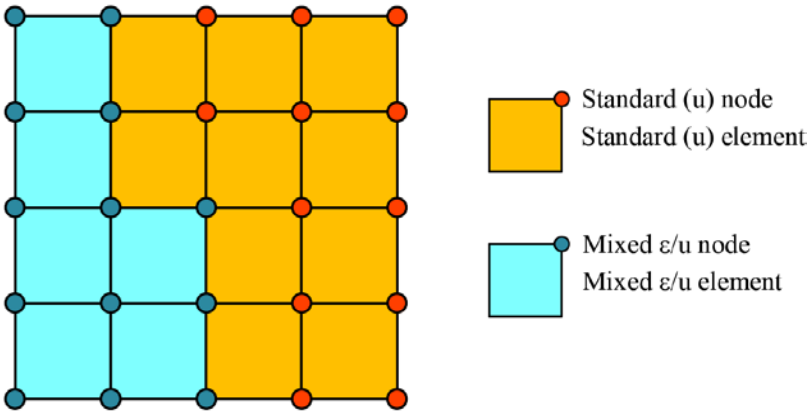

Figure 2. Finite element mesh combining standard and mixed formulations

Strain and stress computations

Strains are computed differently when using the standard and mixed FE formulation. For this reason, when introducing the AFR technique, the consistency of the strain (and stress) fields computed with both formulations needs be addressed.

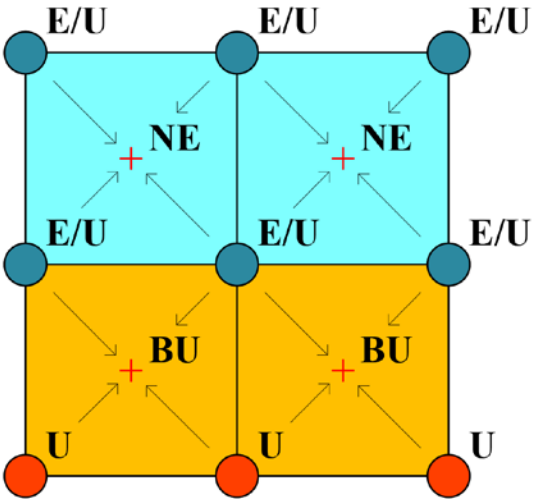

Figure 3. Computation of strains at integration points (represented with red crosses)

As indicated in Figure 3, in the standard displacement-based formulation, strains are evaluated at the integration points through local differentiation at element level using the nodal displacements

$$\boldsymbol{\varepsilon} \cong \hat{\boldsymbol{\varepsilon}} = \mathbf{S}\hat{\boldsymbol{u}} = \mathbf{S}\boldsymbol{N}_u\boldsymbol{U} = \boldsymbol{B}_u\boldsymbol{U} \tag{24}$$

Then, stresses are locally computed using these strains according to the constitutive law of the material.

Contrariwise, in the mixed formulation, strains are additional primary unknowns, calculated at the nodes. Then, the strains at the integration points are computed through the interpolation of the nodal values, as shown in Figure 3, and stresses are also computed locally

$$\boldsymbol{\varepsilon} \cong \hat{\boldsymbol{\varepsilon}} = \boldsymbol{N}_\varepsilon\boldsymbol{E} + \tau_\varepsilon(\boldsymbol{B}_u\boldsymbol{U} - \boldsymbol{N}_\varepsilon\boldsymbol{E}) = (1-\tau_\varepsilon)\boldsymbol{N}_\varepsilon\boldsymbol{E} + \tau_\varepsilon\boldsymbol{B}_u\boldsymbol{U} \tag{25}$$

Refinement criterion

Several refinement criteria may be adopted in the AFR strategy. The general requirements that these need to fulfill are:

1. To be adaptively applicable: the criterion should not require the a priori definition of the domains in which standard and mixed formulations are active. The areas of standard and mixed formulations should be automatically defined by the criterion.
2. To allow decision on both *formulation refinement*, switching from standard to mixed, and *formulation derefinement*, reversal from mixed to standard.
3. To designate the areas of standard and mixed formulations in an accurate and efficient manner: to reduce as much as possible the extent of the mixed formulation while preserving it in the required regions.

The criterion adopted to switch between the standard and mixed formulations is established in terms of the equivalent effective stress $\bar{\sigma}_{eq}$, introduced in the damage constitutive law in Section 2. In the present work the Rankine and Drucker-Prager criteria are adopted and $\bar{\sigma}_{eq}$ is determined according to Eqs. (19) and (20) respectively. Then, the ratio R is defined as

$$R = \frac{\bar{\sigma}_{eq}}{f_t} \tag{26}$$

where f_t is the tensile strength of the material.

If the ratio R exceeds a certain limit α_{max} (e.g. 75%), the mixed formulation is activated. Also, when R drops below a certain threshold α_{min} (e.g. 20 %), the standard formulation is recovered. The switching back from mixed to the standard formulation is not allowed in elements where damage has developed. Therefore, the criterion can be expressed as

$$\begin{aligned} &IF\ \bar{\sigma}_{eq} \geq \alpha_{max} f_t && \rightarrow \quad Activation\ of\ mixed\ FE \\ &IF\ \bar{\sigma}_{eq} < \alpha_{min} f_t \quad AND \quad d = 0 && \rightarrow \quad Activation\ of\ standard\ FE \end{aligned} \tag{27}$$

This AFR criterion automatically defines the regions where the standard and mixed formulations are activated. If in an element the refinement criterion is fulfilled in *one* of the integration points, the whole element is treated as mixed and the strain degrees of freedom are activated in all its nodes. Conversely, if in *all* the integration points of an element the derefinement criterion is met, the standard formulation is reactivated for that particular element. Note that the criterion allows the possibility of having several distinct subdomains with standard and mixed elements. Note also that in the original work [20] formulation derefinement was not contemplated.

Adaptive formulation solution approach

The approach employed to solve the problem with Adaptive Formulation Refinement is the following. According to the proposed refinement criterion, an array indicating for each node which degrees of freedom are active and inactive is updated at each time-step. Elemental matrices are computed and assembled in function of the active formulation. If in a certain node the mixed formulation is active, both displacement and strain degrees of freedom are considered. Instead, if the standard formulation is active, the strain degrees of freedom are not activated and only the displacement degrees of freedom are taken into consideration. In this strategy, all the nodes in the interface are treated as mixed, as can be seen in Figure 2. The proposed methodology does not require additional considerations for interface nodes; contributions from different elements are simply assembled in the standard manner.

The solver stores the global matrix in a compressed format. In this way, only the non-zero entries of the matrix, which are located in function of its graph, are considered. The graph of the matrix is built by DOFs, according to the array labeling the active degrees of freedom of the problem. As demonstrated in reference [20], this approach greatly reduces the computational time involved, as only the active degrees of freedom are considered when building and solving the problem. This method is applicable both for direct and iterative solvers.

3.2. Adaptive mesh refinement

The AMR strategy is included to further increase the efficiency of the model for fracture conferred by the AFR approach. The AMR method allows to begin the computation with an initial relatively coarse mesh requiring a low calculation effort. The mesh is progressively adaptively refined only in the regions where cracks progress to suitably represent the phenomenon of fracture while the coarse mesh is maintained elsewhere. The AMR methodology also includes the subsequent adaptive mesh coarsening of the undamaged elements after the crack has already appeared in the area. An octree refinement strategy is employed, according to the methodology described in references [26-29]. In problems where the crack trajectories are not known a priori this approach avoids the need for initial fine meshes to calculate fracture.

Refinement criterion

A similar refinement criterion as in AFR, based on the same ratio R between the equivalent effective stress $\bar{\sigma}_{eq}$ and the material tensile strength f_t, as defined by Eq. (26), is adopted for ARM. If the ratio R exceeds a certain designated limit β_{max} (e.g. 50%), the mesh is refined. Also, if the ratio R decreases below another set value β_{min} (e.g. 10%), coarsening takes place. Refinement may take place up to a certain predetermined level. Coarsening is not allowed in damaged elements. Hence, the criterion can be stated in the following way:

$$\begin{aligned} &IF\ \bar{\sigma}_{eq} \geq \beta_{max} f_t && \rightarrow \quad Mesh\ refinement \\ &IF\ \bar{\sigma}_{eq} < \beta_{min} f_t \quad AND \quad d = 0 && \rightarrow \quad Mesh\ coarsening \end{aligned} \tag{28}$$

Note that the values of the thresholds introduced for the refinement criteria in AMR and AFR in the numerical simulations may be different. This means that AMR and AFR may be activated independently, depending on the selected α_{min}, α_{max}, β_{min}, β_{max} parameters.

Analogously to AFR, mesh refinement takes place in an element if the refinement criterion is reached in *one* of the integration points; an additional refinement level is introduced at every time step until the predefined maximum number of refinement levels is attained. Contrarily, coarsening occurs if *all* the integration points of the element meet the coarsening criterion.

Adaptive finite element approach

In the following, a brief overview of the FE adaptivity strategy employed is provided. For additional details, references [26-29] are recommended.

The hierarchical octree refinement strategy defines several levels of FEs, represented in Figures 4 and 5. The original FEs are labeled with the level zero and are the parents to the level one FEs (which are the children of the zero level FEs). Level one FEs are the parents of level two FEs, etc.

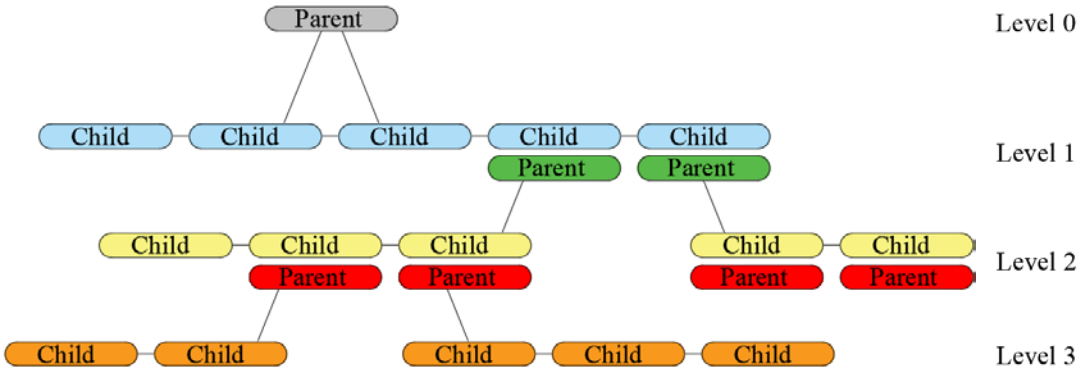

Figure 4. Finite element hierarchy in the octree-based AMR strategy

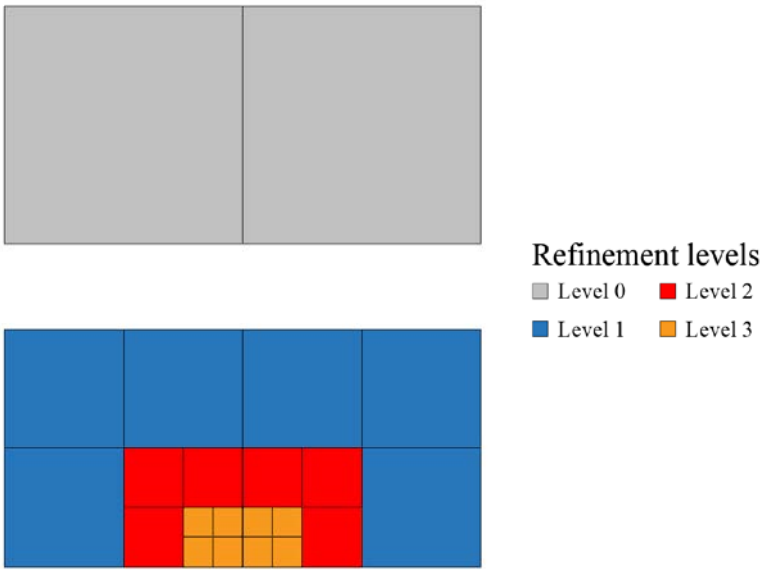

Figure 5. Depiction of the octree-based refinement process in a finite element

When a new mesh is generated during the AMR process, the information from the previous mesh is projected onto the new one. The nodal displacements of existing nodes are preserved. The values corresponding to new nodes are interpolated from the values of existing nodes. If the mixed FE formulation is active for the parent element, the same procedure is followed for the nodal strain field. The historical variables of the damage constitutive law of new nodes are set to the values corresponding to the initially undamaged material. Since coarsening is allowed only in undamaged elements, no loss of information related to the historical variables of the nonlinear constitutive behavior occurs. Setting proper limits for the refinement criterion also avoids the refinement of already damaged elements. With regard to the combination of AMR with AFR, the array indicating which degrees of freedom are active and inactive for each node is then updated.

The presence of hanging nodes in the octree refined FE mesh, depicted in Figure 6, needs to be properly treated. In the present work, the treatment of hanging nodes proposed in references [26, 27] is followed. According to this approach, the following modification of the shape functions of the parent elements is performed when hanging nodes are present so that the FE approximation becomes conforming:

$$\boldsymbol{N}_p^*(\boldsymbol{x}) = \boldsymbol{N}_p(\boldsymbol{x}) + \sum_{i=1}^{n_{child}} \boldsymbol{N}_p(\boldsymbol{x}_i)\boldsymbol{N}_{c,i}(\boldsymbol{x}) \tag{29}$$

where $\boldsymbol{N}_p$ and $\boldsymbol{N}_p^*$ are the original and modified parent interpolation functions, $\boldsymbol{N}_c$ are the original children interpolation function, n_{child} is the number of hanging children nodes and $\boldsymbol{x}_i$ indicates the position of hanging child i. The degrees of freedom of hanging nodes are eliminated from the FE system being solved. Their contributions are added to the nodes of the parent elements according to the modified shape functions, Eq. (29). The values of the unknowns at the hanging nodes are obtained by interpolation from nodes of the parent element. Additional details are provided in the original references [26, 27].

The combination of the AFR and AMR methodologies is fairly straightforward and does not require special additional considerations.

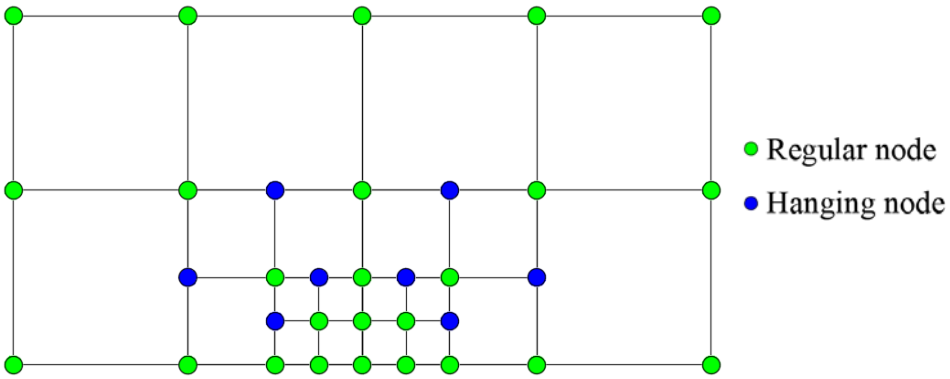

Figure 6. Regular and hanging nodes in the FE mesh

4. Numerical simulation of quasi-brittle structural failure

In this section the numerical simulation of experimental tests and benchmark case studies reported in the literature featuring quasi-brittle structural failure is performed using the proposed model including mesh and FE formulation adaptivity. The selected cases are often employed for the validation of numerical models.

The objectives of this section are (i) to demonstrate the mesh objectivity of the proposed model based on the AFR and AMR approaches, (ii) to assess the cost-efficiency of the proposed method compared to the standard displacement-based FEs as well as the non-adaptive mixed FEs, (iii) to show proper convergence of the results to the appropriate solution.

The computations are performed with an enhanced version of the finite element code FEMUSS while pre- and post- processing are performed with GID [50], both developed at the International Center for Numerical Methods in Engineering (CIMNE). Convergence in each load step is attained when the ratio between the norm of residual forces and the norm of total external forces is lower than 10^{-5}.

4.1. Garcia-Alvarez beams

In this section, the numerical simulation of the Garcia-Alvarez experiments, reported in reference [51], is performed. The work [51] includes the computational modelling of the tests using interface elements. This problem has also been simulated with the phase-field regularized cohesive zone model (PF-CZM) by Wu and coworkers [52]. In previous works the results obtained using mixed FE have been compared with the experiments [15] and with phase-field based computations [6, 53].

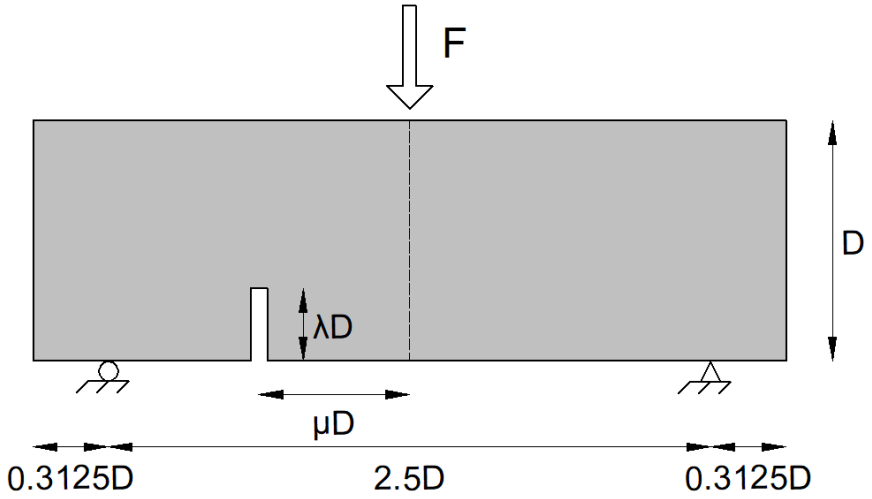

Figure 7. Geometry of the Garcia-Alvarez beams

Young's Modulus	$33.8 \cdot 10^9$ Pa
Poisson's Ratio	0.2
Tensile Strength	$3.5 \cdot 10^6$ Pa
Tensile Fracture Energy	80 J/m^2

Table 1. Material parameters of the Garcia-Alvarez beams

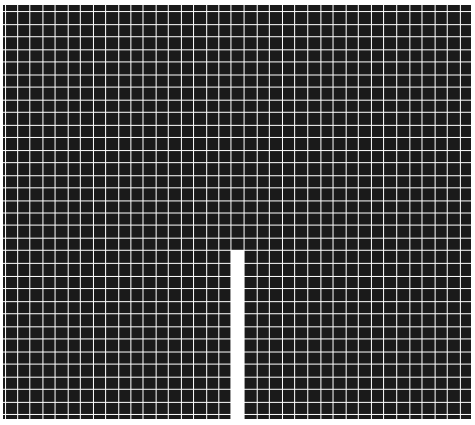

Figure 8. Detail of the initial mesh used for the Garcia-Alvarez beams in the area of the notch

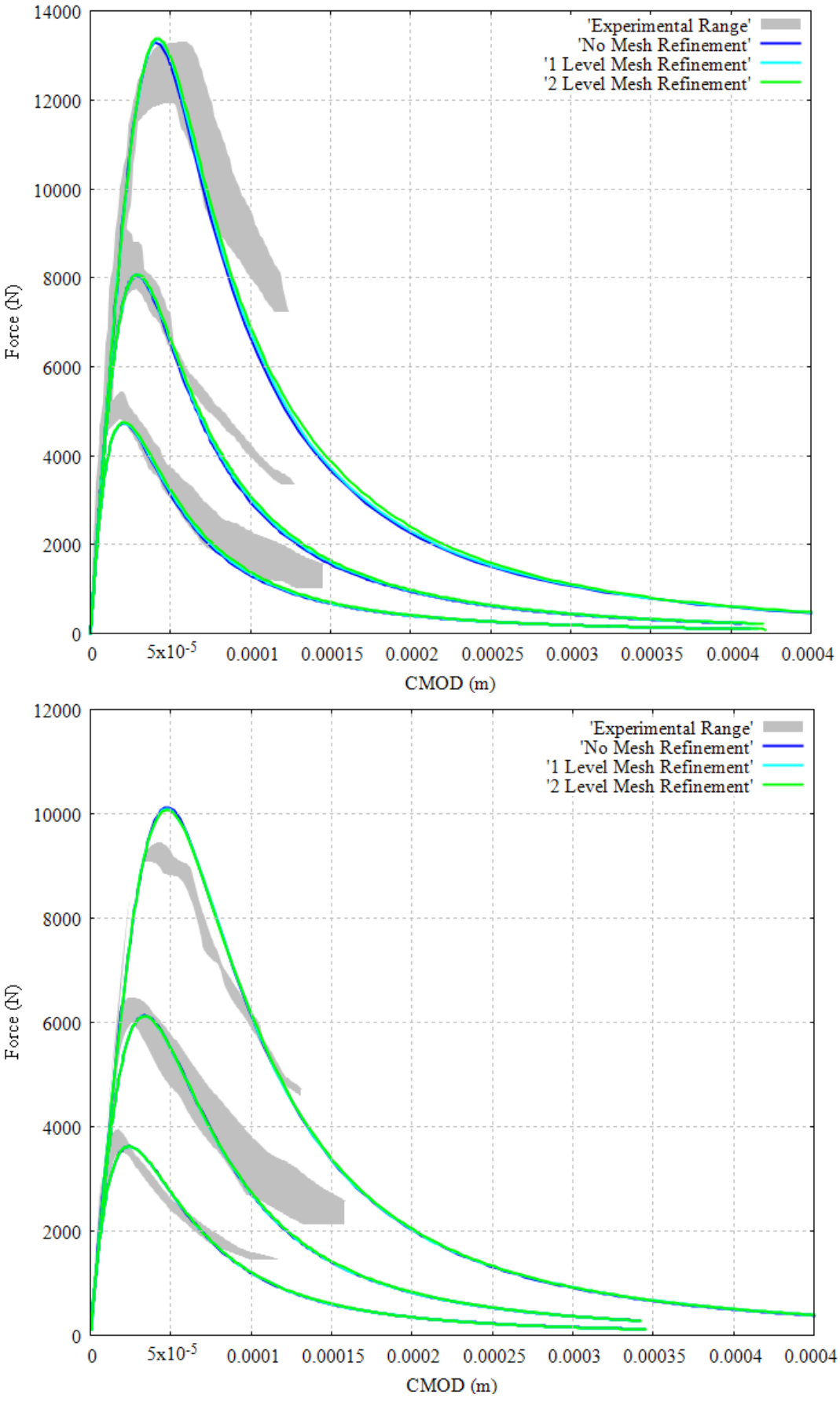

Figure 9. Force-displacement curves of the Garcia-Alvarez beams for the 3 sizes using different levels of adaptive mesh refinement. Eccentricities (top) 0.625D and (bottom) 0.3125D

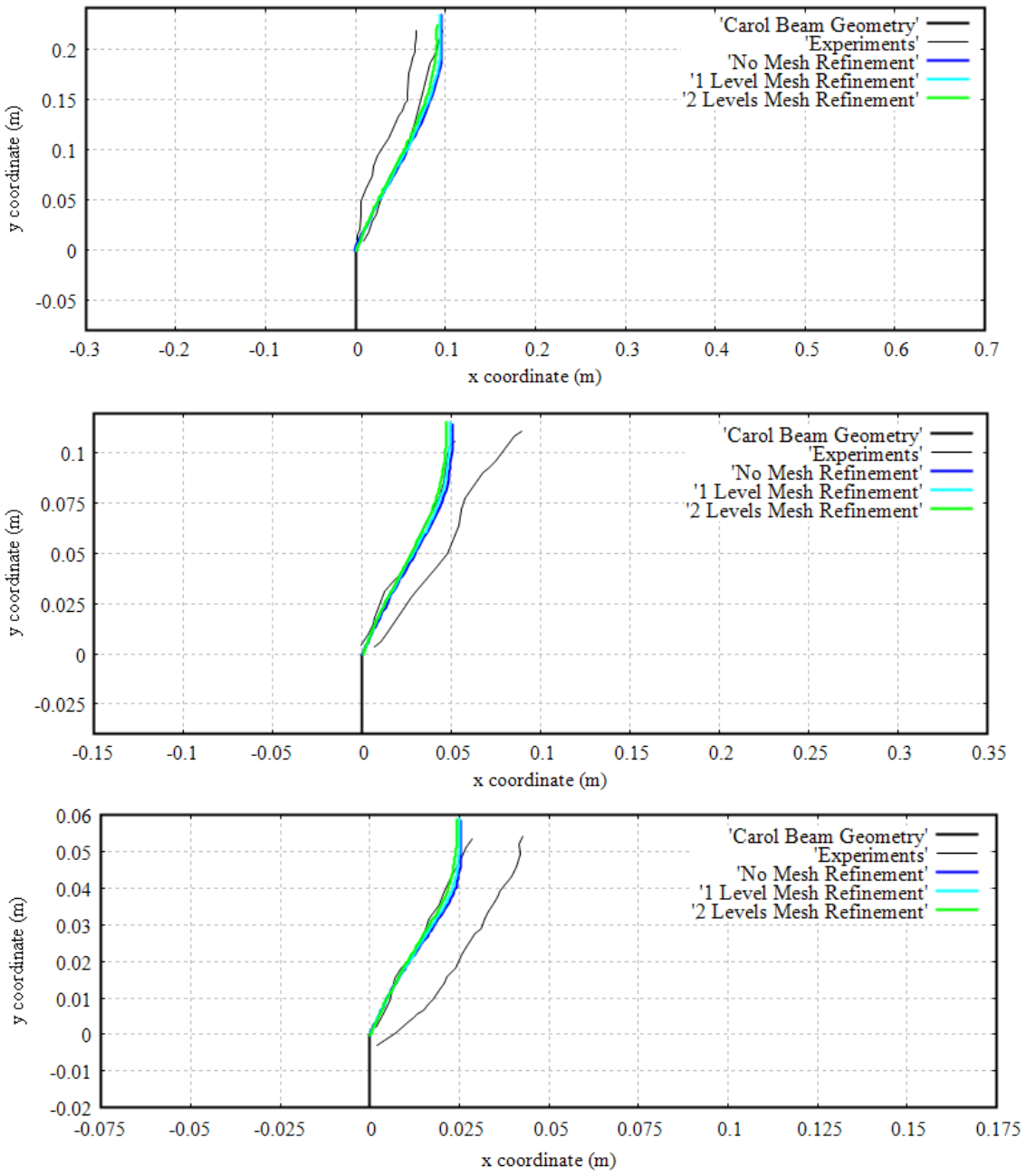

Figure 10. Computed crack trajectories of the Garcia-Alvarez beams with different levels of mesh refinement, eccentricity 0.625D, for sizes (top) D = 320 mm, (center) D = 160 mm and (bottom) D = 80 mm

In these experiments, geometrically similar beams of different sizes are subjected to three-point bending tests in order to study the structural size effect. The geometry of the beams is detailed in Figure 7. Three different structural sizes are considered: beams with depths D of 320 mm, 160 mm and 80 mm. A constant span-to-depth ratio of 2.5 is taken. In the experiments three different series are considered, by varying the position of the notch in the specimen, so that mixed-mode fracture occurs. Specifically, notch eccentricities μD of $0.625D$, $0.3125D$ and $0.0D$ were used. The thickness of the beams in all the cases is 50 mm. A vertical force was applied at the top midpoint of the beams as indicated in Figure 7. The computational simulations are performed under CMOD control, reproducing the conditions of the experiment. Table 1 shows the material properties used for the beams, together with the Rankine damage surface.

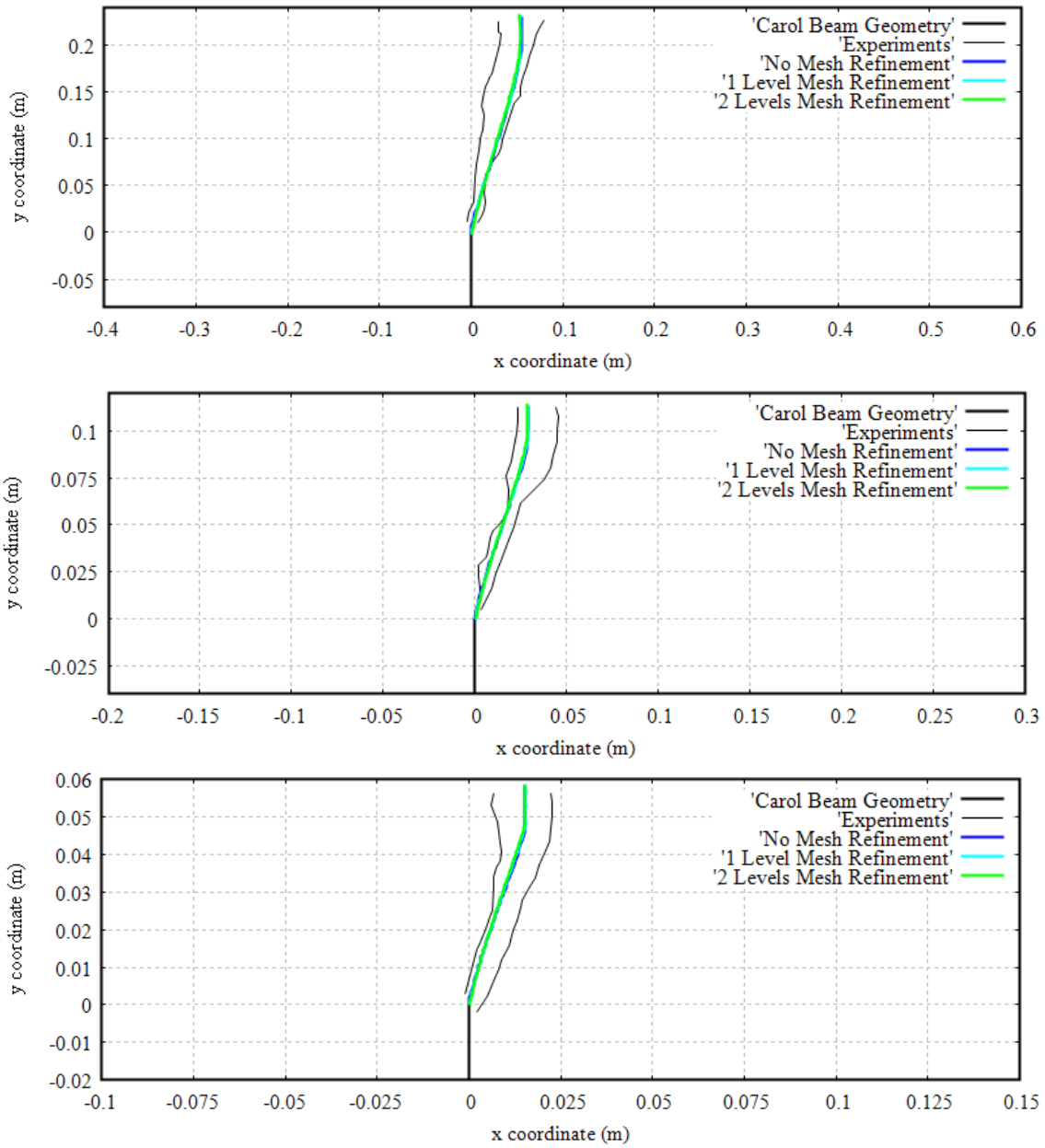

Figure 11. Computed crack trajectories of the Garcia-Alvarez beams with different levels of mesh refinement, eccentricity 0.3125D, for sizes (top) D = 320 mm, (center) D = 160 mm and (bottom) D = 80 mm

The objective of this section is to validate the proposed AMR and AFR capabilities introduced in this work. For this, the numerical simulation of the series with notch eccentricities μD of $0.625D$ and $0.3125D$ is performed, with concurrent adaptive FE formulation refinement and different levels of adaptive mesh refinement, up to 2 levels.

The initial meshes adopted to perform the simulation, for the two eccentricity cases and all the sizes, have approximately 31,000 elements, resulting from using a mesh size h of $10^{-2}D$. The notch is modelled with thickness h, as is shown in Figure 8. The original mesh is fine enough to obtain satisfactory results; it is chosen to show that proper convergence occurs with different levels of adaptive mesh refinement.

In Figure 9, the force-displacement curves computed for the two series and for all the sizes are shown. It can be seen that the results with the different levels of adaptive mesh refinement (from no mesh refinement to 2 levels of mesh refinement) are practically overlapping. This shows that

results have reached convergence in terms of mesh size. All results compare well with the experiments for all the sizes and for all the cases. This is remarkable, as for all the simulations the same material properties are used. This confirms the results in reference [15] where the ability of the mixed finite element method in reproducing the structural size effect is demonstrated.

Figures 10 and 11 compares the computed crack trajectories for all the sizes of the two beam series with the corresponding experiments. It can be seen that all the numerical results are within the experimental range. The simulations with the different levels of mesh refinement considered are practically matching, demonstrating that convergence of the results has been achieved. No sign of spurious mesh dependence is observed when using the AFR method combining standard and mixed FEs.

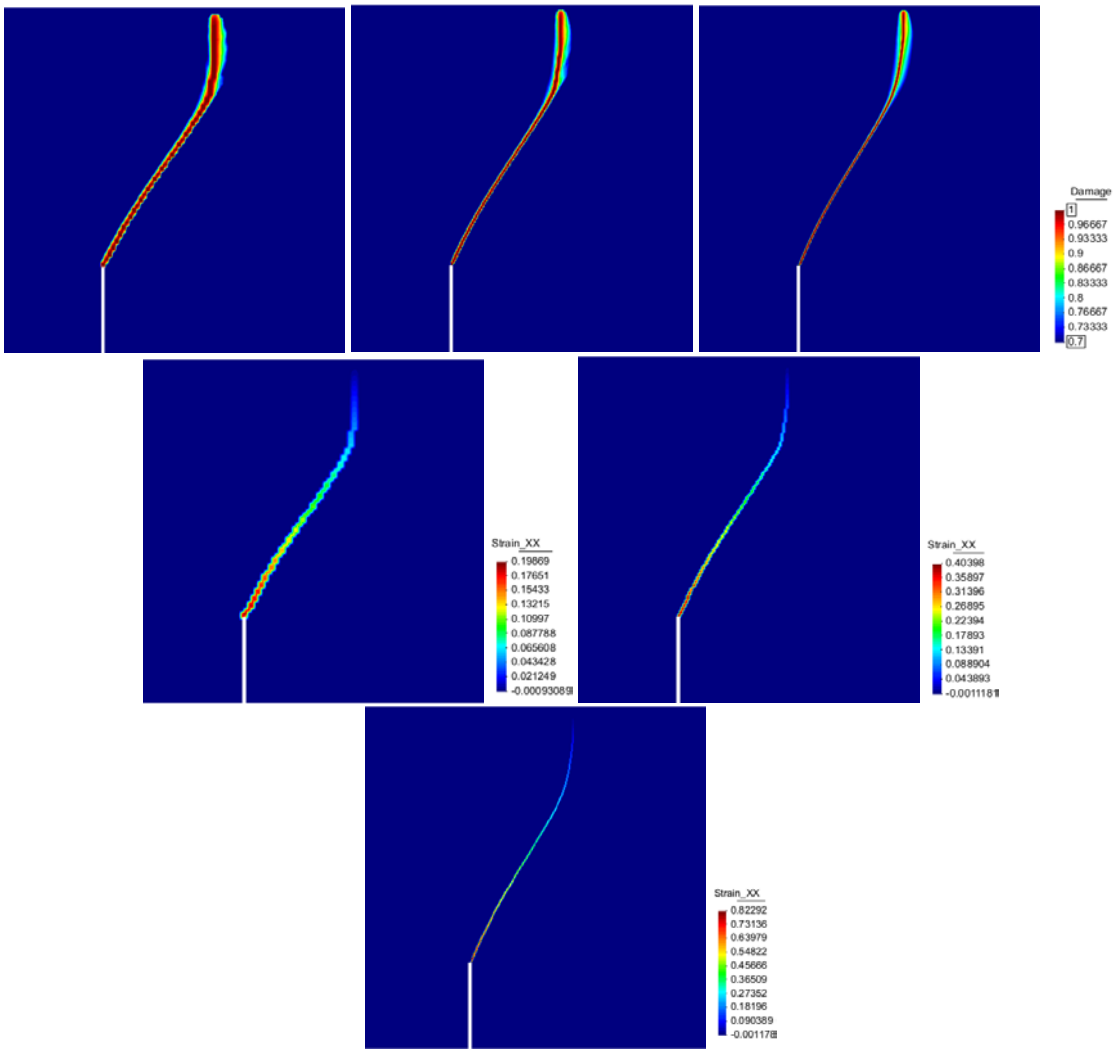

Figure 12. Computed (top) damage and (bottom) strain contours of the Garcia-Alvarez beams, D = 80 mm specimen, eccentricity 0.625D series, with (left) no AMR, (center) 1 level of AMR and (right) 2 levels of AMR

In Figure 12 the computed damage and strain fields for the $D = 80\,mm$ sized specimen, eccentricity $0.625D$, are displayed. A comparison between results obtained with (i) no AMR, (ii) 1 level of AMR and (iii) 2 level of AMR is made. In all cases, damage is plotted within the range that matches the corresponding localizing strains. It can be seen both in the damage and strain fields how the crack bandwidth is reduced when the FE size decreases. Notwithstanding, the correct energy dissipation with respect to the FE size is enforced by the Crack Band Theory,

as it can be seen in the force-displacement curves in Figure 9; also, practically the same crack trajectories are obtained, as shown in Figure 10.

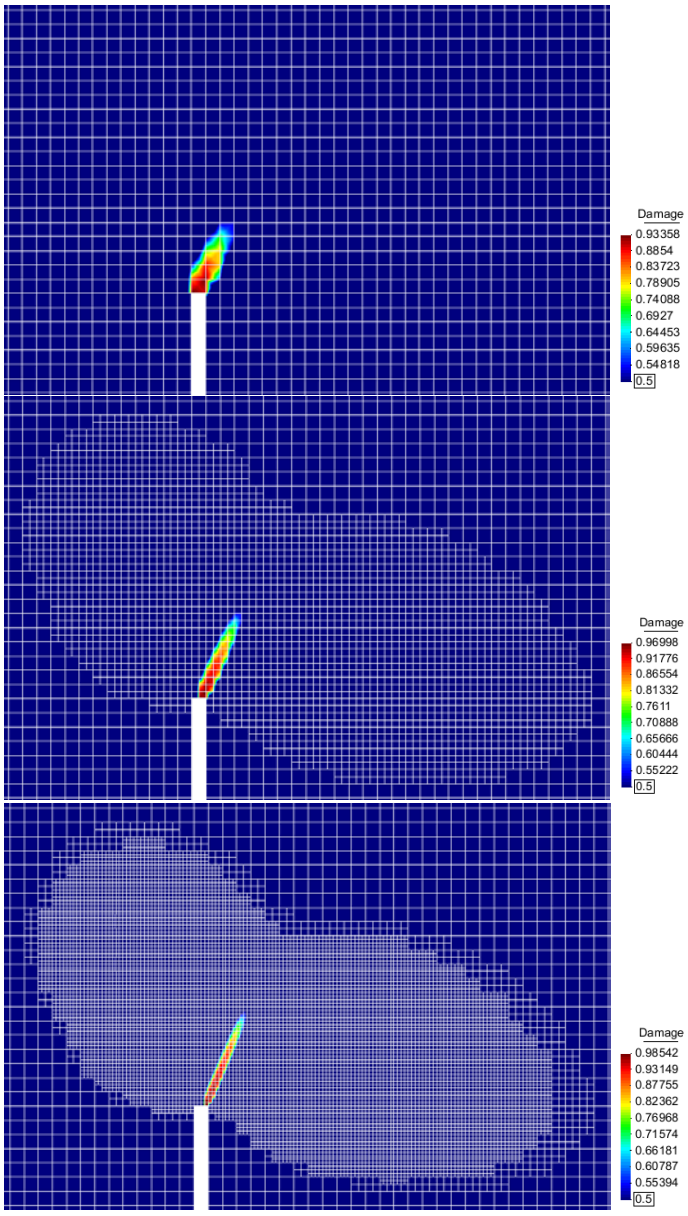

Figure 13. Computed damage contour with the detail of the mesh in the notched region at the early stages of the simulation with (top) no AMR, (center) 1 level of AMR and (bottom) 2 levels of AMR

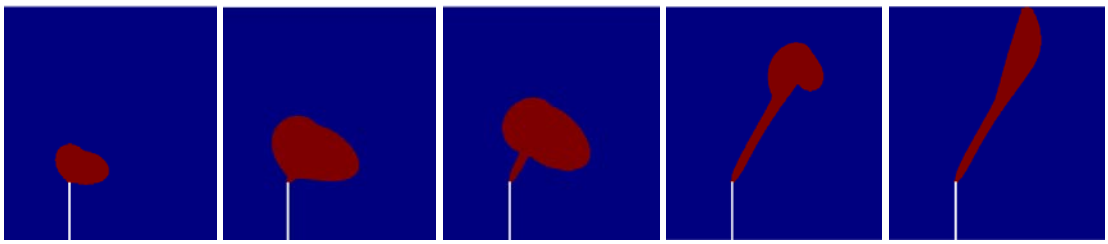

Figure 14. Evolution of the area where standard (in blue) and mixed (in red) formulations are adopted during the simulation with 2 levels of AMR of the Garcia-Alvarez beams, eccentricity 0.625D, D = 80 mm

Figure 13 shows the detail of the FE mesh in the region of the notch at the early stages of the simulation without AMR and with 1 and 2 levels of AMR. It can be seen how the FE mesh is refined only in the area where the crack progresses according to the adaptive mesh refinement criterion defined in Section 3.

In the computations of the Garcia-Alvarez beams, mesh refinement takes place when the equivalent effective stress $\bar{\sigma}_{eq}$ reaches a value higher than $0.5f_t$ and coarsening occurs when $\bar{\sigma}_{eq}$ attains a value lower than $0.1f_t$.

Figure 14 shows the evolution of the area where standard and mixed FE formulations are active for different time steps of the simulation of the Garcia-Alvarez beam, $D = 80\,mm$ sized specimen, eccentricity $0.625D$. With the criterion defined in Section 3, mixed $\boldsymbol{\varepsilon/u}$ FEs are activated only in a small region near the developing crack.

In all the simulations of the Garcia-Alvarez beams, formulation refinement, i.e. activation of the mixed $\boldsymbol{\varepsilon/u}$ FE, occurs when the equivalent effective stress $\bar{\sigma}_{eq}$ reaches a value higher than $0.75f_t$. Formulation derefinement, i.e. deactivation of the mixed $\boldsymbol{\varepsilon/u}$ FE, takes place when $\bar{\sigma}_{eq}$ attains a value lower than $0.2f_t$; no switching from mixed to standard takes place in damaged elements.

In Table 2 the details of the reduction in computational cost by the adaptive formulation refinement methodology are indicated for the $D = 80\,mm$ and eccentricity $0.625D$ case. Similar values are obtained for all the other cases of the Garcia-Alvarez beams. For each of the cases considered (without AMR, with 1 level of AMR and with 2 levels of AMR) the first three columns compare the maximum number of degrees of freedom (labelled Max. Ndofs) ensuing from computations with standard FE only, mixed FE only, and the proposed AFR strategy. The last two columns show the relation between the Max. Ndofs resulting from the use of AFR with respect to the corresponding values of standard FE only and mixed FE only computations.

In 2D and 3D simulations, the ratio of unknowns between the standard and mixed FE formulations is 33.33%. This means that the lowest possible value that can be reached in the fourth column of Table 2 for the percentage of Max. Ndofs using AFR with respect the a mixed only calculation is 33.33%. Note that the actual values indicated in the column are very close to this lower bound, demonstrating the efficiency of the proposed approach. The fifth column of Table 2 indicates the relation between the Max. Ndofs using AFR with respect the standard only analysis, which is very close in all the cases to the lower possible value of 100%. The use of the AFR allows to decisively reduce the number of degrees of freedom, and therefore the computational cost, of the simulation with respect to the use of the mixed $\boldsymbol{\varepsilon/u}$ formulation. In fact, the maximum number of degrees of freedom required with AFR is slightly larger than that of using the standard FE formulation.

	Max. Ndofs standard FEs	Max. Ndofs mixed $\boldsymbol{\varepsilon/u}$ FEs	Max. Ndofs AFR	% of Ndofs with respect to mixed only	% of Ndofs with respect to standard only
Without AMR	63,226	189,678	71,222	37.55%	**112.65%**
1 level of AMR	89,196	267,588	100,012	37.38%	**112.13%**
2 levels of AMR	190,926	572,778	229,870	40.13%	**120.40%**

Table 2. Cost-efficiency of the proposed mesh and formulation adaptivity scheme for the Garcia-Alvarez beams

	Number of nodes with	Max. number of	%

	initial uniform refinement	nodes with AMR	
No mesh refinement	31,613	-	-
1 level of refinement	125,575	44,598	**35.52%**
2 levels of refinement	500,549	95,463	**19.07%**

Table 3. Cost-efficiency of the proposed mesh adaptivity scheme for the Garcia-Alvarez beams

Table 3 further details the cost-effectiveness of the proposed mesh adaptivity scheme for the numerical simulation of quasi-brittle fracture. For each of the cases considered (without refinement, with 1 level of refinement and with 2 levels of refinement) the first column indicates the number of nodes that ensue from performing an initial uniform refinement of the mesh and the second column displays the number of nodes resulting from the adoption of the AMR strategy. The third column presents the relation between the two previous values. It can be seen how the adopted AMR scheme substantially reduces the number of nodes, and therefore the computational cost, of the simulation with respect to the alternative of performing an initial uniform refinement of the mesh.

The calculations show that: (i) a large reduction in computational cost by the use of the adaptive FE formulation capabilities is achieved, (ii) results are convergent when different levels of adaptive mesh refinement are considered, both in terms of crack trajectories and force-displacement curves, (iii) results agree with the experiments and do not exhibit any sign of spurious mesh dependency, (iv) the quasi-brittle fracture model based on the adoption of the mixed strain/displacement FE method is able of reproducing structural size effect with accuracy.

4.1.1. Comparison with standard FE simulations

In the following, results obtained using standard FEs only are compared with the ones of the previous section. The objective is to demonstrate that mesh refinement by itself is not able to yield satisfactory results; the use of mixed $\boldsymbol{\varepsilon/u}$ FEs is necessary for that purpose. In this section the specimen with $D = 80\,mm$ and eccentricity $0.625D$ is considered only. The same initial mesh and material properties are employed.

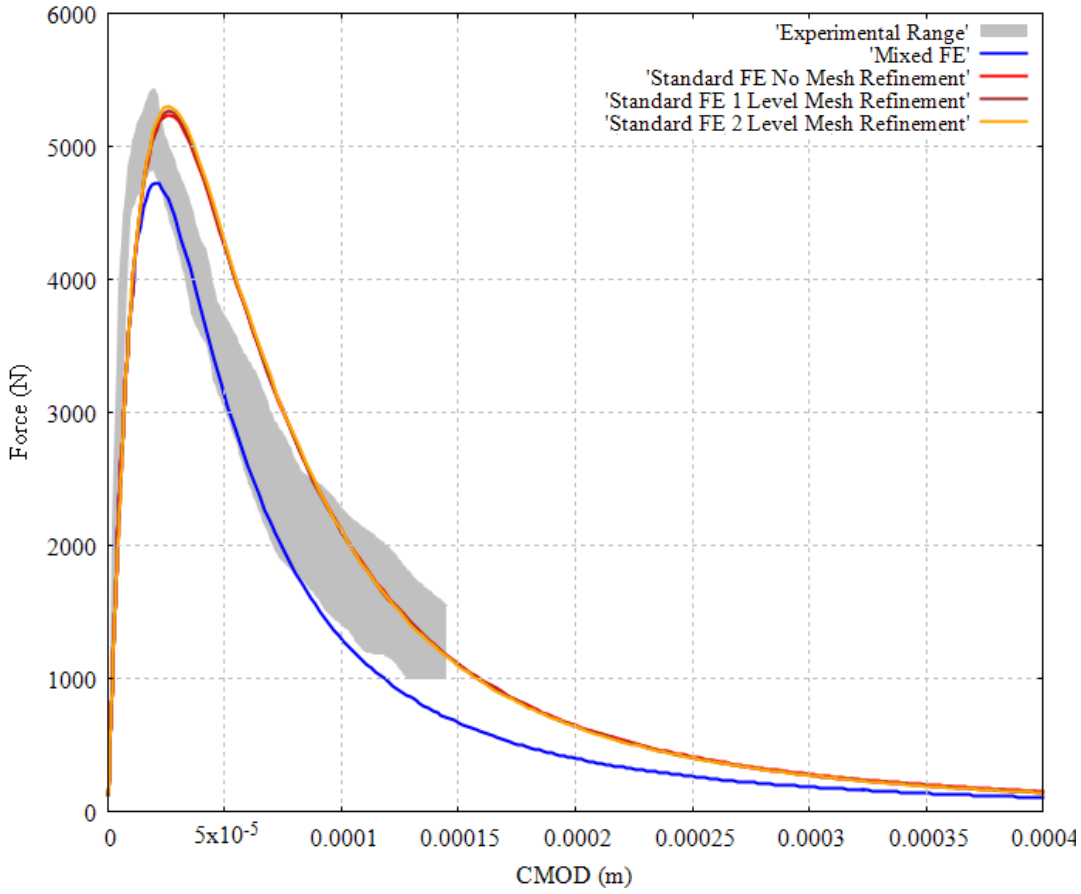

Figure 15. Force-displacement curves of the Garcia-Alvarez beams, standard FEs, using different levels of adaptive mesh refinement. D = 80 mm specimen and eccentricity 0.625D

Figure 15 shows the force-displacement curves computed with standard FEs using different levels of AMR. It can be observed that, despite the fact that the solutions computed with standard FEs are practically overlapping, they converge to a different force-displacement curve than mixed FEs.

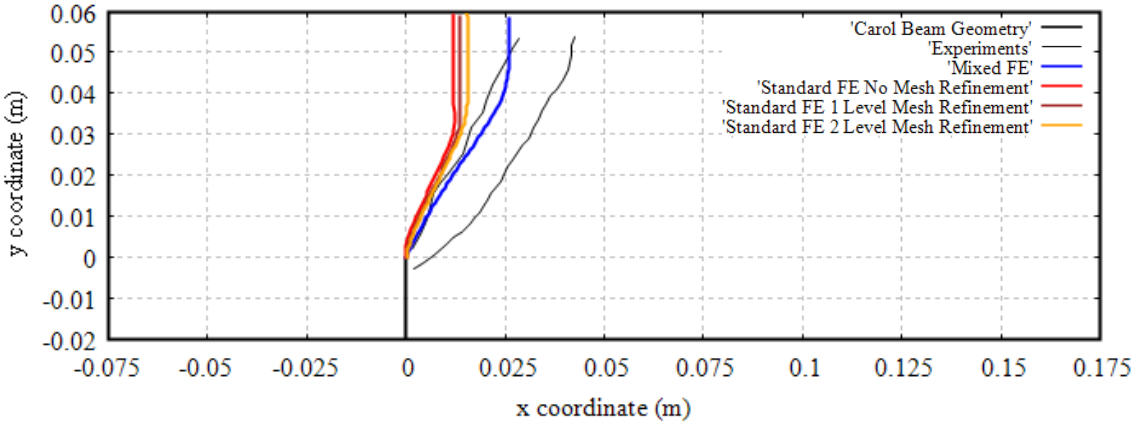

Figure 16. Computed crack trajectories of the Garcia-Alvarez beams, standard FEs, using different levels of adaptive mesh refinement. D = 80 mm specimen and eccentricity 0.625D

In Figure 16, the crack trajectories computed with standard FEs are shown. The crack trajectories vary when different levels of mesh refinement are adopted, showing spurious mesh bias dependency and non-convergent results. Also, fractures calculated with standard FEs are

outside the experimental range. The large difference between the crack trajectories obtained with standard and mixed FEs is the reason for obtaining different solutions in terms of force-displacement curves as well, the difference between the two calculated peak loads being of 11%.

Figure 17 displays the computed damage and maximum principal strain fields using standard FEs, comparing the results without AMR and with 1 and 2 levels of AMR. Again, it can be seen how the crack bandwidth diminishes as the FE size decreases. Despite the fact that the resulting force-displacement curves are converging to the same solution when using standard FEs, showing that the correct energy dissipation with respect to the FE size is enforced by the Crack Band Theory, the computed results are different in terms of crack trajectory, as shown in Figure 16.

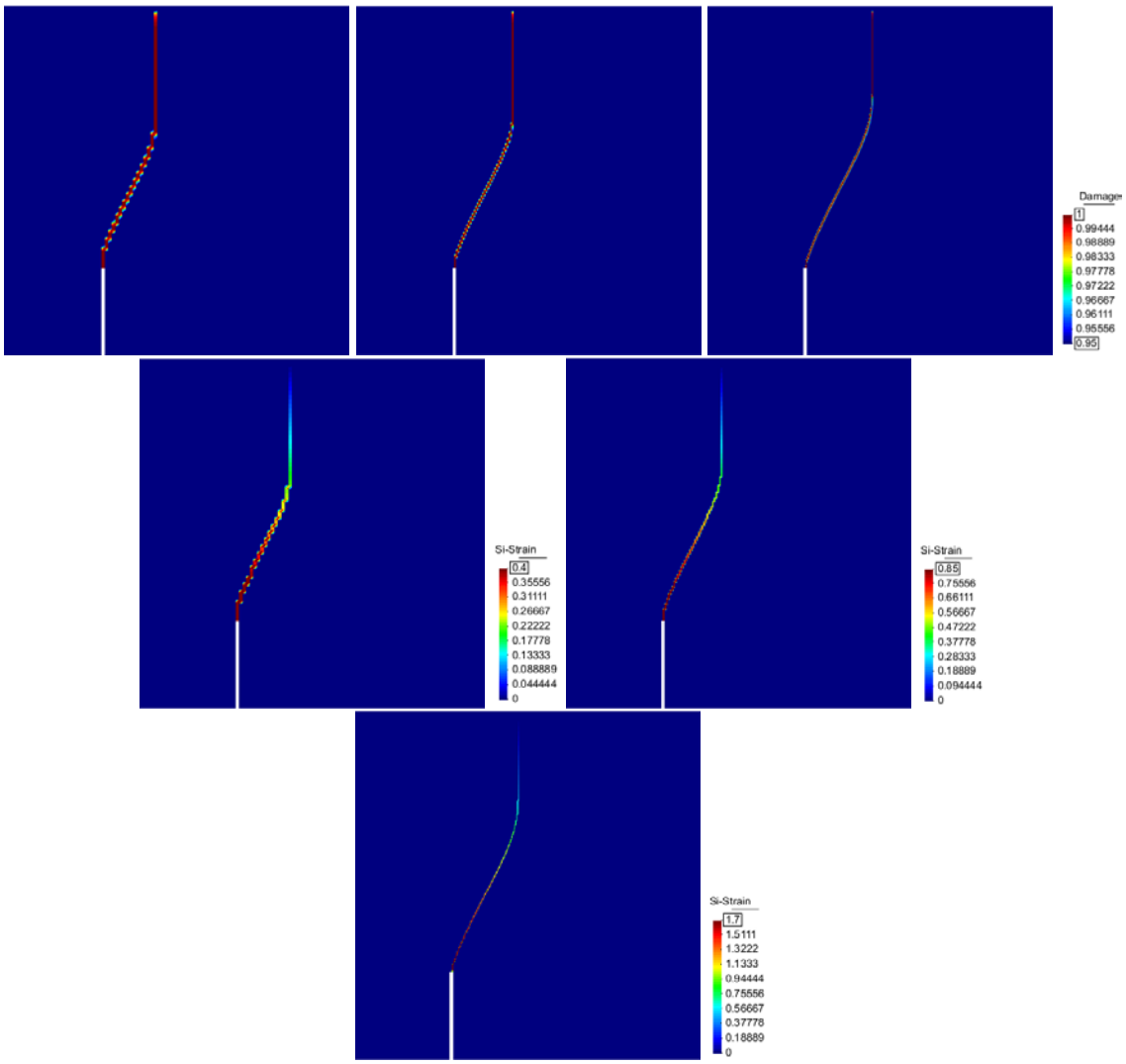

Figure 17. Computed (top) damage and (bottom) maximum principal strain contours using standard FEs, D = 80 mm specimen, eccentricity 0.625D series, with (left) no AMR, (center) 1 level of AMR and (right) 2 levels of AMR

4.2. Arrea and Ingraffea beam

This section presents the numerical simulation of the Arrea and Ingraffea mixed mode bending test, reported in reference [54]. As reference [6] details, this experiment has been numerically modelled many times using several different approaches to crack modelling.

The geometry and the boundary conditions of the beam are indicated in Figure 18a. The eccentricity of the applied loading with respect to the notch results in the mixed mode of the fracture. The beam has dimensions of 0.914 m x 0.305 m and a notch length of 82.4 mm. The beam thickness is 0.152 m. Two eccentric loads of values F and 0.13F act on the upper surface. The material properties considered are indicated in Table 4. The Drucker-Prager damage surface is considered for the damage constitutive law in this case. The numerical simulations are performed under Crack Mouth Sliding Displacement (CMSD) control.

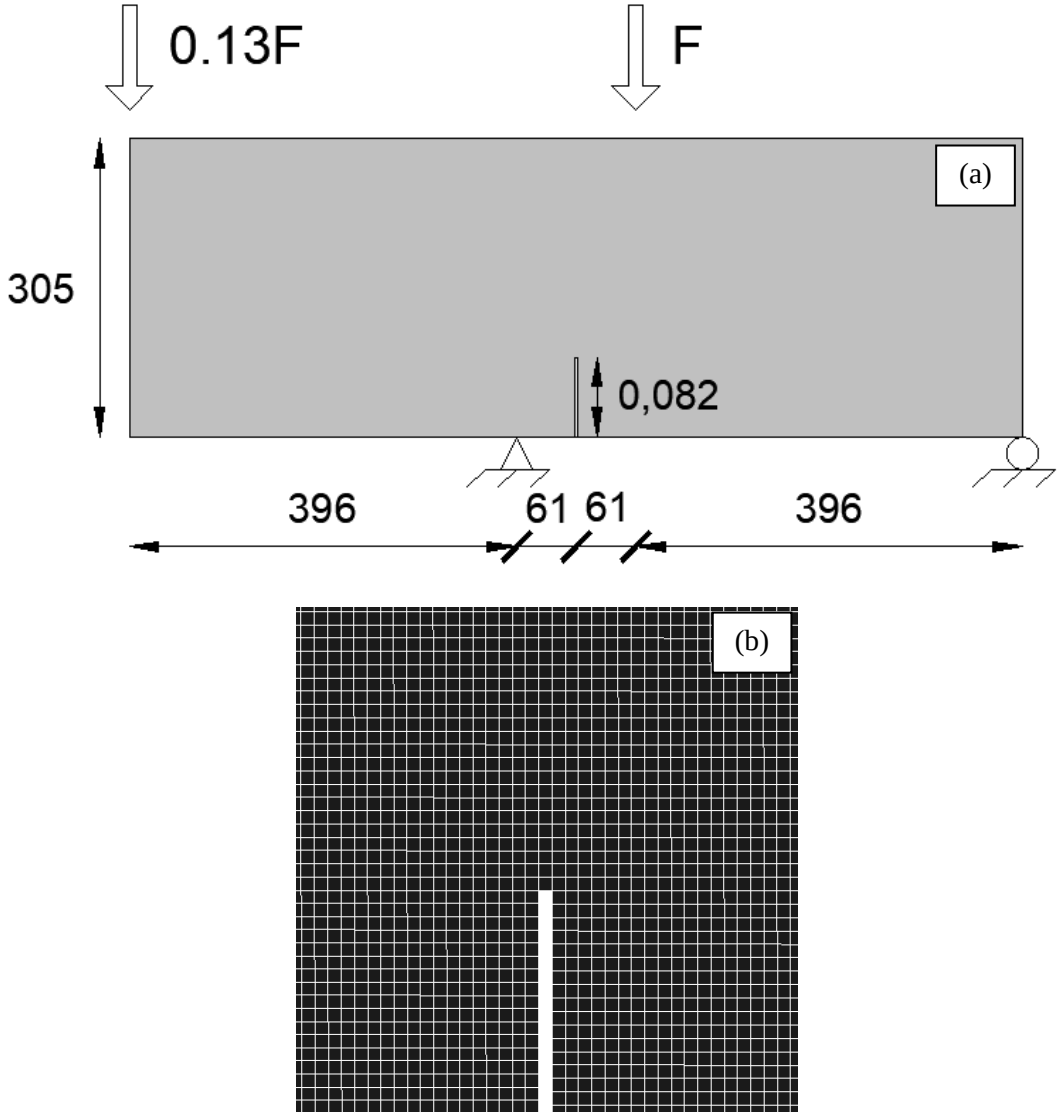

Figure 18. Arrea and Ingraffea beam: (a) Geometry (mm) and (b) detail of the mesh in the area of the notch

Young's Modulus	$28.8 \cdot 10^9$ Pa
Poisson's Ratio	0.18
Tensile Strength	$3.7 \cdot 10^6$ Pa
Tensile Fracture Energy	130 J/m^2
Compressive Strength	$43.4 \cdot 10^6$ Pa

Table 4. Material parameters of the Arrea and Ingraffea beam

The objective of this section is to validate the proposed methodology through comparison with the experimental results. To this end, the present case study examines the results of the numerical simulations obtained with (i) no mesh refinement, (ii) 1 level of adaptive mesh refinement and (iii) 2 levels of adaptive mesh refinement. AMR takes place when the equivalent effective stress $\bar{\sigma}_{eq} \geq 0.5 f_t$. The coarsening of the mesh is decided when $\bar{\sigma}_{eq} \leq 0.1 f_t$. In all the cases, the adaptive formulation refinement capabilities are introduced as well. The mixed formulation is activated if $\bar{\sigma}_{eq} \geq 0.75 f_t$ and the standard formulation is reestablished if $\bar{\sigma}_{eq} \leq 0.5 f_t$.

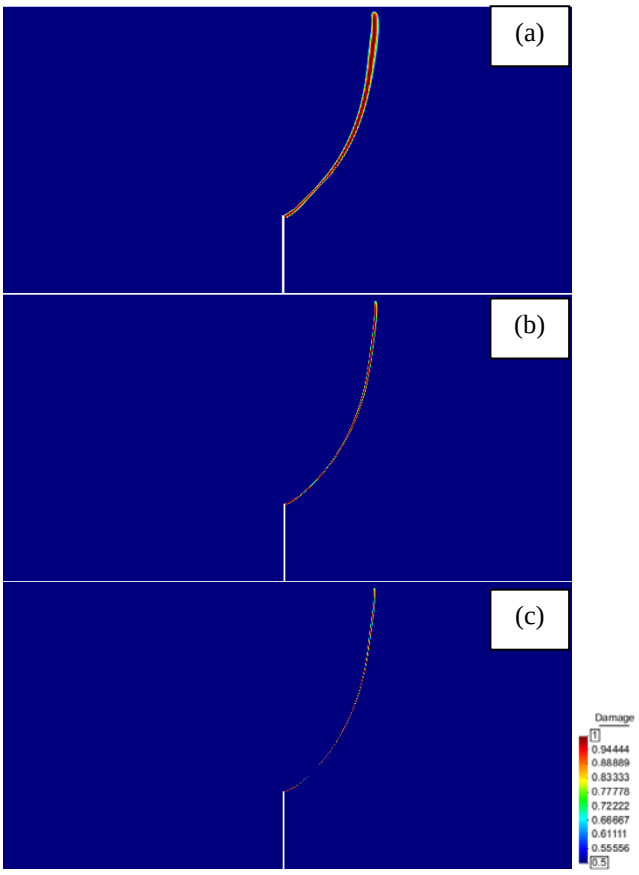

Figure 19. Computed damage contours of the Arrea and Ingraffea beam with: (a) no AMR, (b) 1 level of AMR and (c) 2 levels of AMR

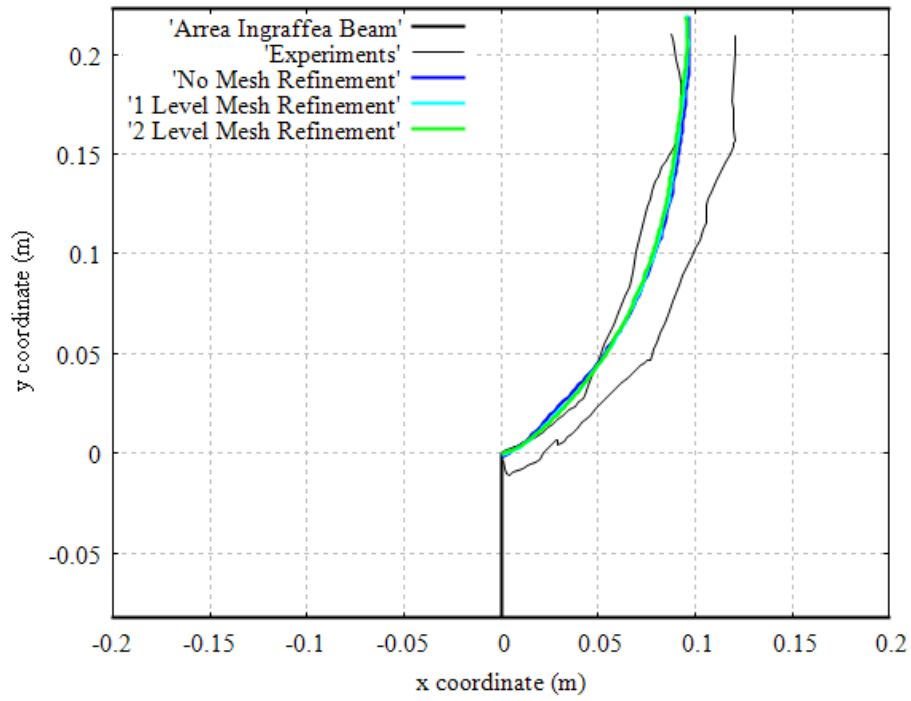

Figure 20. Detail of the computed crack trajectories for the different levels of mesh refinement of the Arrea and Ingraffea beam

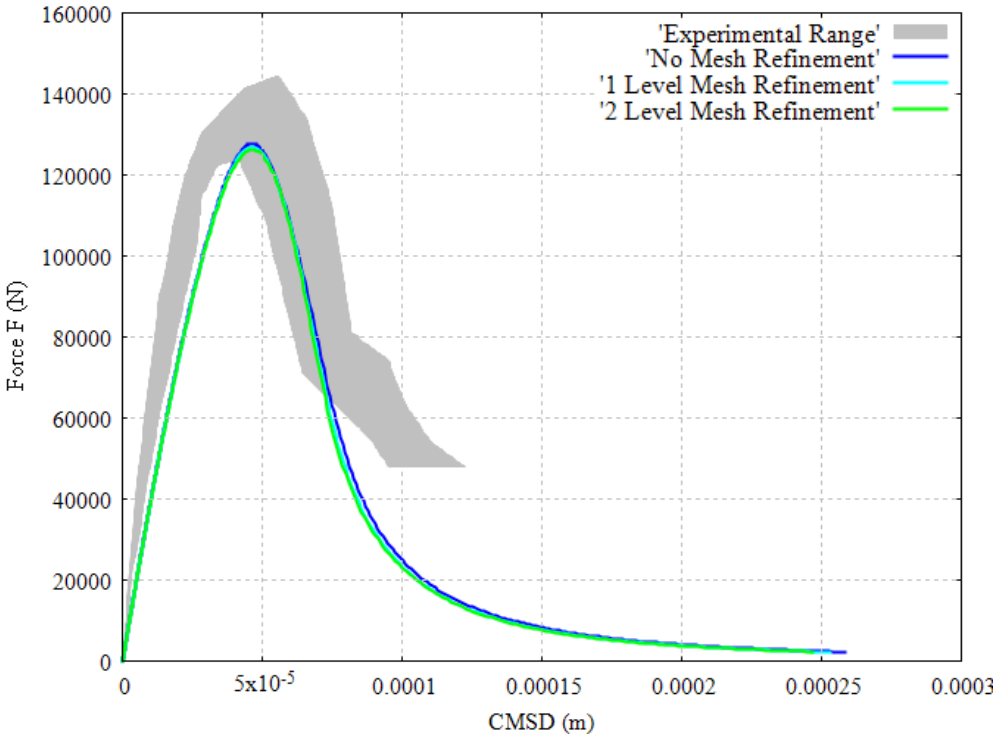

Figure 21. Computed Force F vs CMSD curves of the Arrea and Ingraffea beam

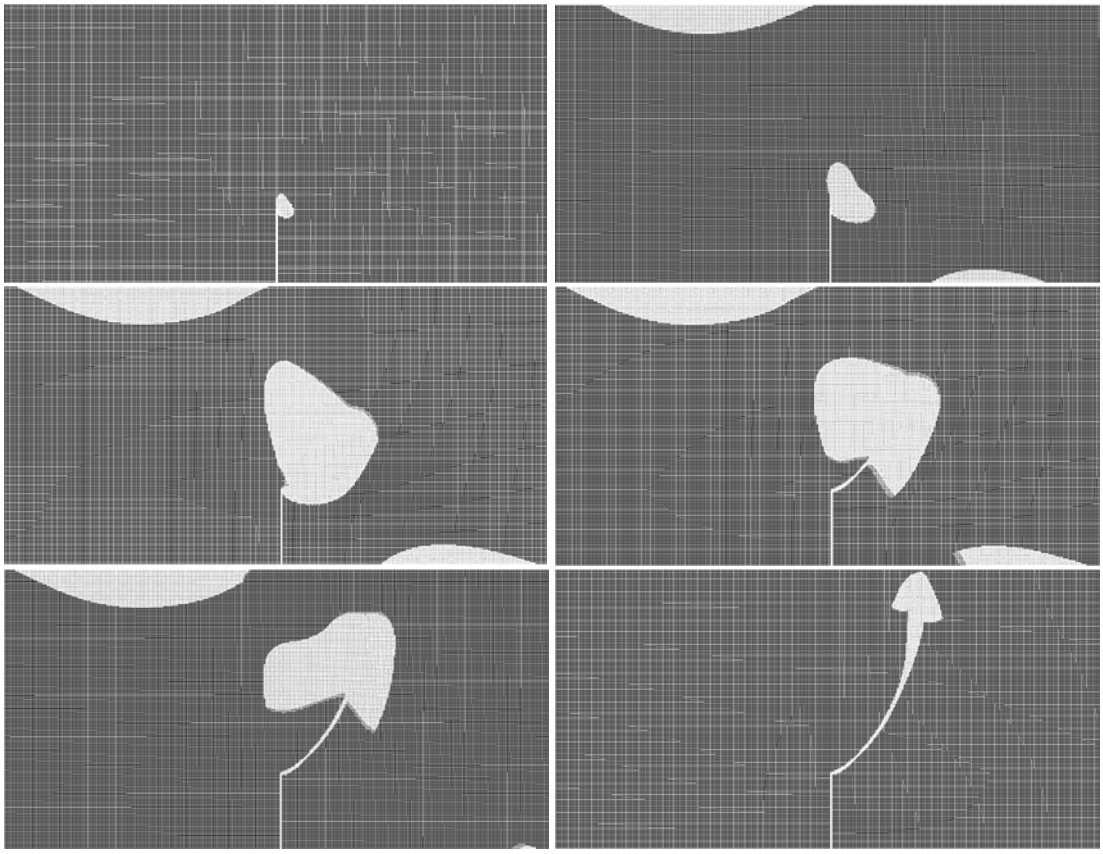

Figure 22. Evolution of the FE mesh during the simulation with 2 levels of AMR of the Arrea and Ingraffea beam

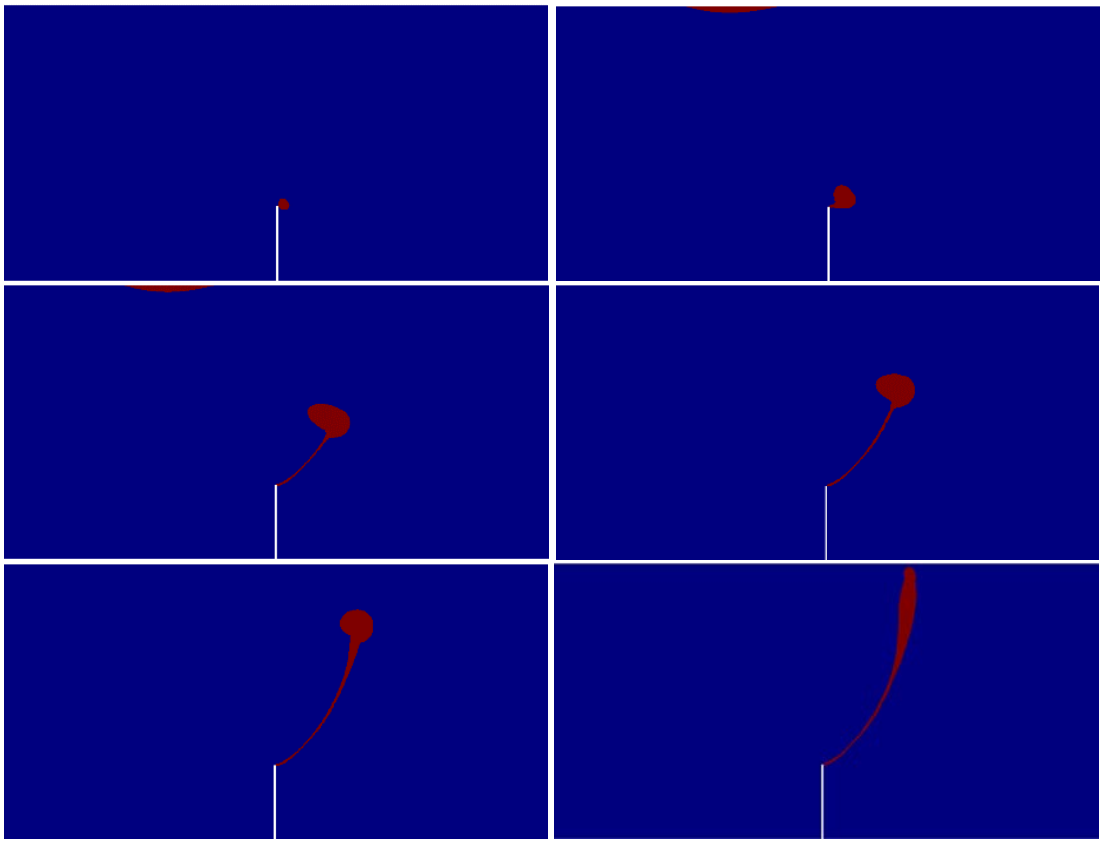

Figure 23. Evolution of the area where standard (in blue) and mixed (in red) formulations are adopted during the simulation with 2 levels of AMR of the Arrea and Ingraffea beam

The initial mesh employed has a FE size of 2 mm. This corresponds to a mesh of 71,761 elements. The notch is modelled with a thickness of 1 finite element, as is shown in Figure 18b. The initial mesh considered in the simulations is fine enough to provide satisfactory results; it is selected to demonstrate that convergence occurs when adaptive mesh refinement is activated.

Figure 19 shows the computed damage contours, comparing results (i) without AMR, (ii) with 1 level of AMR and (iii) with 2 levels of AMR. The crack, starting at the notch, gradually turns and modifies its trajectory due to the mixed mode loading conditions of the test. The detail of the crack trajectories is examined in Figure 20. On the one hand, it can be seen how the numerical results are practically overlapping and that convergence of the solution is properly taking place upon mesh refinement. On the other hand, the crack trajectories obtained with the adaptive FE formulation method proposed in this work matches the experimental observations.

In Figure 21 the computed Force F vs CMSD curves with the different levels of mesh refinement are displayed. It can be seen again that proper convergence of the solution is taking place as well when considering the force-displacement response. The computations agree with the experimental observations both in terms of bearing capacity and of overall nonlinear behavior.

Figure 22 shows the evolution of the FE mesh during the simulation as a result of the adaptive mesh refinement capabilities introduced in the model. In Figure 23 the evolution of the areas where standard and mixed FEs are active during the simulation is presented. The ability of the criterion based on $\bar{\sigma}_{eq}$ to allow the correct switching between standard and mixed formulations effectively is verified again.

In Table 5 the cost-efficiency of the proposed AFR scheme is assessed. For the three cases considered (without AMR, with 1 level of AMR and with 2 levels of AMR), the first three columns provide the maximum number of degrees of freedom (Max. Ndofs) involved in the computations using standard FE only, mixed FE only and AFR respectively. The last two columns indicate the relation between the Max. Ndofs in AFR with respect to the other two approaches, (standard only and mixed only). The analyzes performed with AFR necessitated a very small increment in the number of degrees of freedom with respect to the use of standard FEs (~5%).

Table 6 presents the cost-effectiveness of the AMR approach. For each of the contemplated cases (without refinement, with 1 level of refinement and with 2 levels of refinement) the first column shows the number of elements resulting from the adoption of a uniform mesh refinement strategy. The second column displays the number of nodes that ensue from the use of the AMR method proposed in this work. The third column details the ratio between the two previous values. It can be observed how the proposed AMR strategy allows for a very significant reduction in the number of elements and therefore the cost of the computational simulations.

	Max. Ndofs standard FEs	Max. Ndofs mixed $\boldsymbol{\varepsilon/u}$ FEs	Max. Ndofs AFR	% of Ndofs with respect to mixed only	% of Ndofs with respect to standard only
Without AMR	144,910	434,730	153,050	35.21%	**105.62%**
1 level of AMR	182,566	547,698	192,786	35.20%	**105.60%**
2 levels of AMR	329,890	989,670	358,350	36.21%	**108.63%**

Table 5. Cost-efficiency of the proposed mesh and formulation adaptivity scheme for the Arrea and Ingraffea beam

	Number of elements with initial uniform refinement	Max. number of elements with AMR	%
No mesh refinement	71,761	-	-
1 level of refinement	287,044	90,724	**31.61%**
2 levels of refinement	1,148,176	164,077	**14.29%**

Table 6. Cost-efficiency of the proposed mesh adaptivity scheme for the Arrea and Ingraffea beam

Computations with the mixed $\boldsymbol{\varepsilon/u}$ FE approach do not present any trace of spurious mesh dependency. The adaptive formulation approach allows to obtain results with enhanced accuracy and mesh objectivity while introducing an extremely reduced increase in the computational cost with respect to the use of standard FEs. The efficiencies displayed by the AFR and AMR methods are caused by the fact that the crack propagates in a reduced area of the whole structure. Only a small portion of the beam reaches the nonlinear regime, as it can be observed in Figures 19, 22 and 23.

4.3. Bocca beam

This section analyzes the capabilities of the proposed model in reproducing the results of the doubly notched beam of the Bocca experiment, reported in reference [55]. Reference [55] includes as well the numerical simulation of the test using an automatic remeshing scheme to reproduce crack propagation.

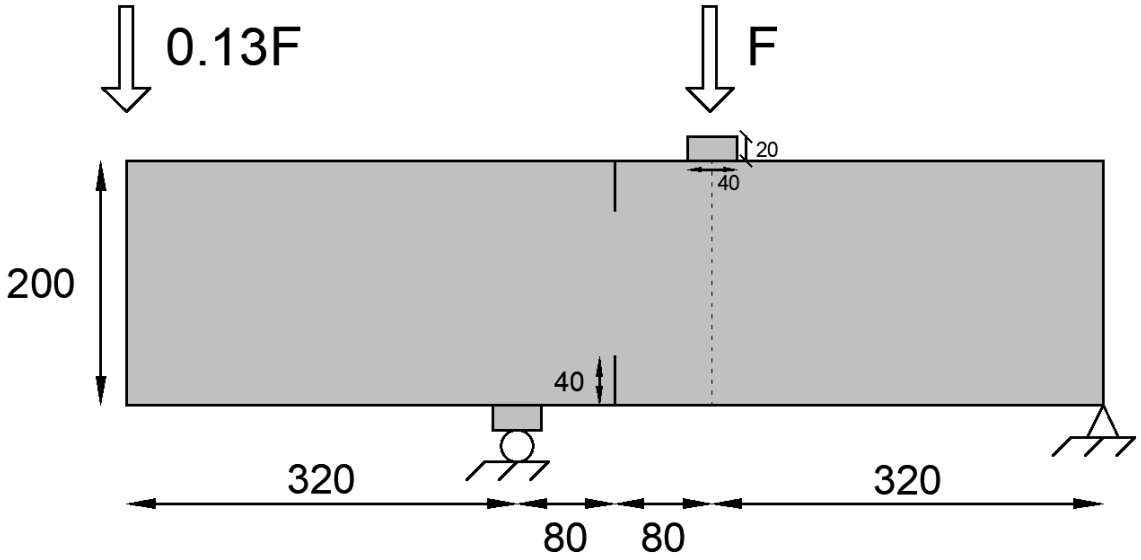

Figure 24. Geometry of the Bocca beam (mm)

Young's Modulus	$27.0 \cdot 10^9$ Pa
Poisson's Ratio	0.18
Tensile Strength	$2.0 \cdot 10^6$ Pa
Tensile Fracture Energy	100 J/m^2
Compressive Strength	$37.3 \cdot 10^6$ Pa

Table 7. Material properties of the Bocca beam

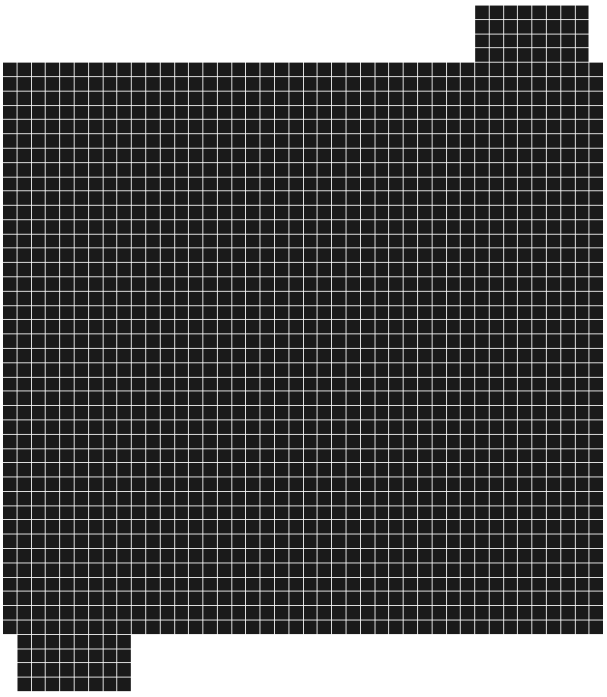

Figure 25. Detail of the initial mesh employed in the analysis of the Bocca beam in the central area

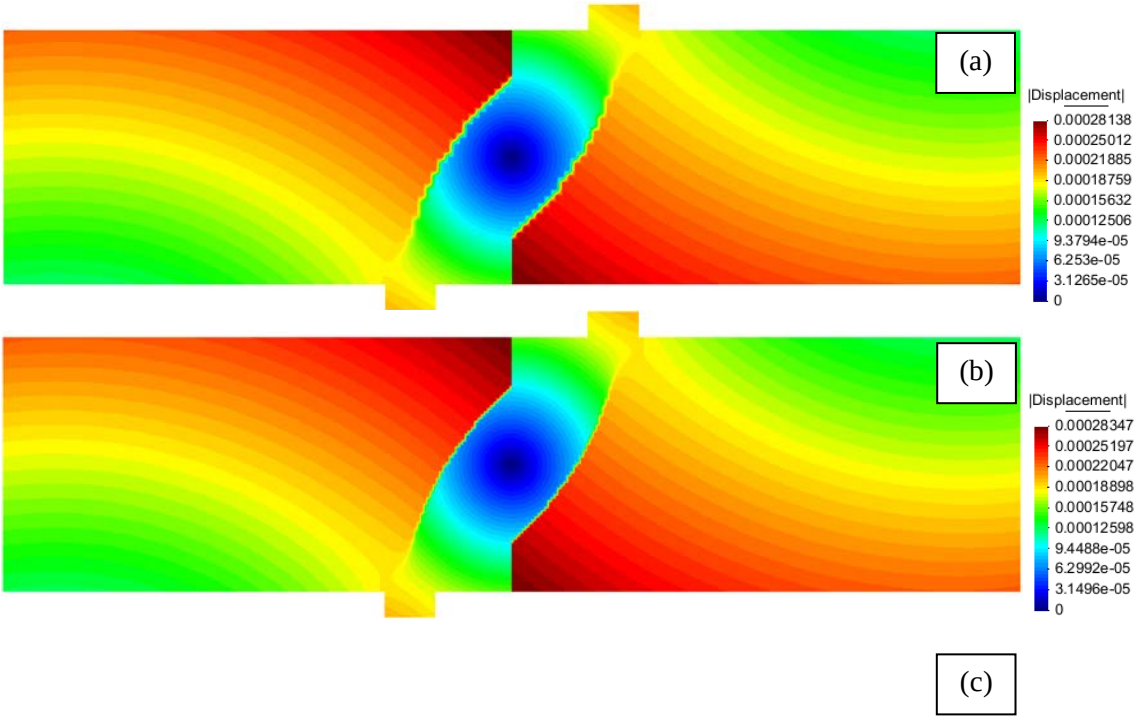

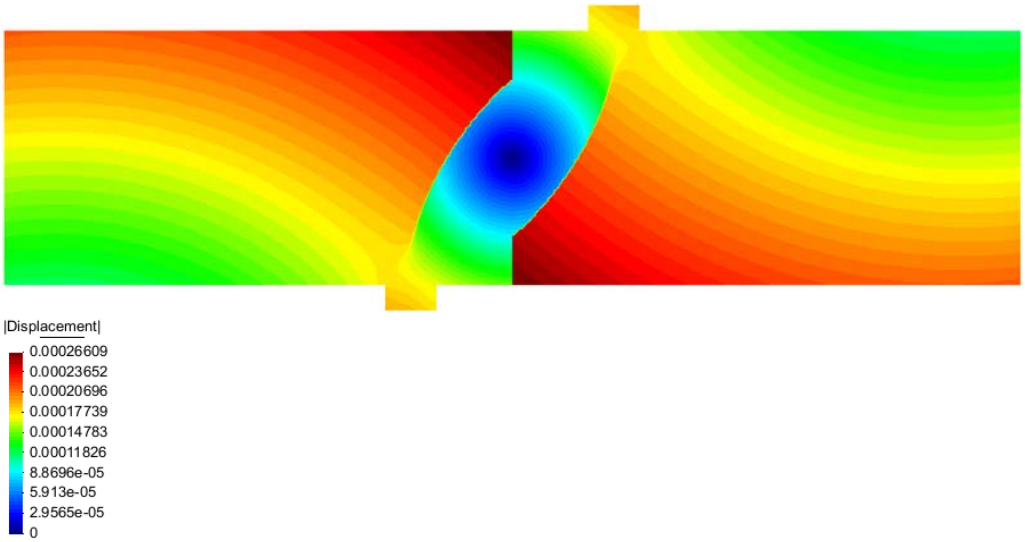

Figure 26. Displacement contours of the Bocca beam with: (a) no AMR, (b) 1 level of AMR and (c) 2 levels of AMR

This problem has been solved in references [56, 57], where particle meshless methods are adopted, in reference [58], where the boundary element method is used, in reference [59], which employed EFEM, in reference [60], where another automatic remeshing scheme is proposed and in reference [61], which introduced a localization limiter to regularize the problem.

The geometry and boundary conditions of the test are detailed in Figure 24. The beam has dimensions 0.8 m x 0.2 m and a thickness of 0.1 m. Two notches of 40 mm length are introduced, and two eccentric forces of values F and 0.2F are applied as detailed in Figure 24. Note that the beam geometry and boundary conditions are polar symmetric. The material parameters are given in Table 7. The Drucker-Prager damage criterion is adopted. The simulation is performed under crack mouth opening displacement (CMOD) control of the upper notch.

In order to assess the proposed AMR and AFR capabilities, a coarse initial mesh in considered for the present case study, and different levels of adaptive mesh refinement are subsequently introduced. The initial mesh, shown in Figure 25, has a FE size of 5 mm, which results in a total of 6,464 elements. This section intends to analyze the capabilities of the model when more than one crack develops.

In this case study, mesh refinement takes place when the equivalent effective stress $\bar{\sigma}_{eq} \geq 0.5 f_t$ and coarsening occurs when $\bar{\sigma}_{eq} \leq 0.25 f_t$. The mixed FE formulation is activated when $\bar{\sigma}_{eq} \geq 0.75 f_t$ and deactivated when $\bar{\sigma}_{eq} \leq 0.25 f_t$.

Figure 26 shows the computed displacement contours of the Bocca beam, where results (i) without AMR, (ii) with 1 level of AMR and (iii) with 2 levels of AMR are contrasted. The position of the cracks can be located due to the high gradient of displacements that they generated. It can be observed how the beam breaks into 3 different pieces, and that the central piece is exhibiting a pure rotation motion, due to the polar symmetry of the applied boundary conditions. Note how the displacement gradients are much more localized when a lower FE size is adopted, due to the adaptive mesh refinement capabilities of the model.

In Figure 27 the computed damage contours of the Bocca beam are shown, comparing results (i) without AMR, (ii) with 1 level of AMR and (iii) with 2 levels of AMR. It can be seen how two cracks with polar symmetry are developing in the beam, as is expected from the applied boundary conditions. Figure 28 examines the detail of the computed crack trajectories. It can be

observed how the three simulations are producing practically overlapping results. Also, note that the computed fractures are inside the range of experimental observations.

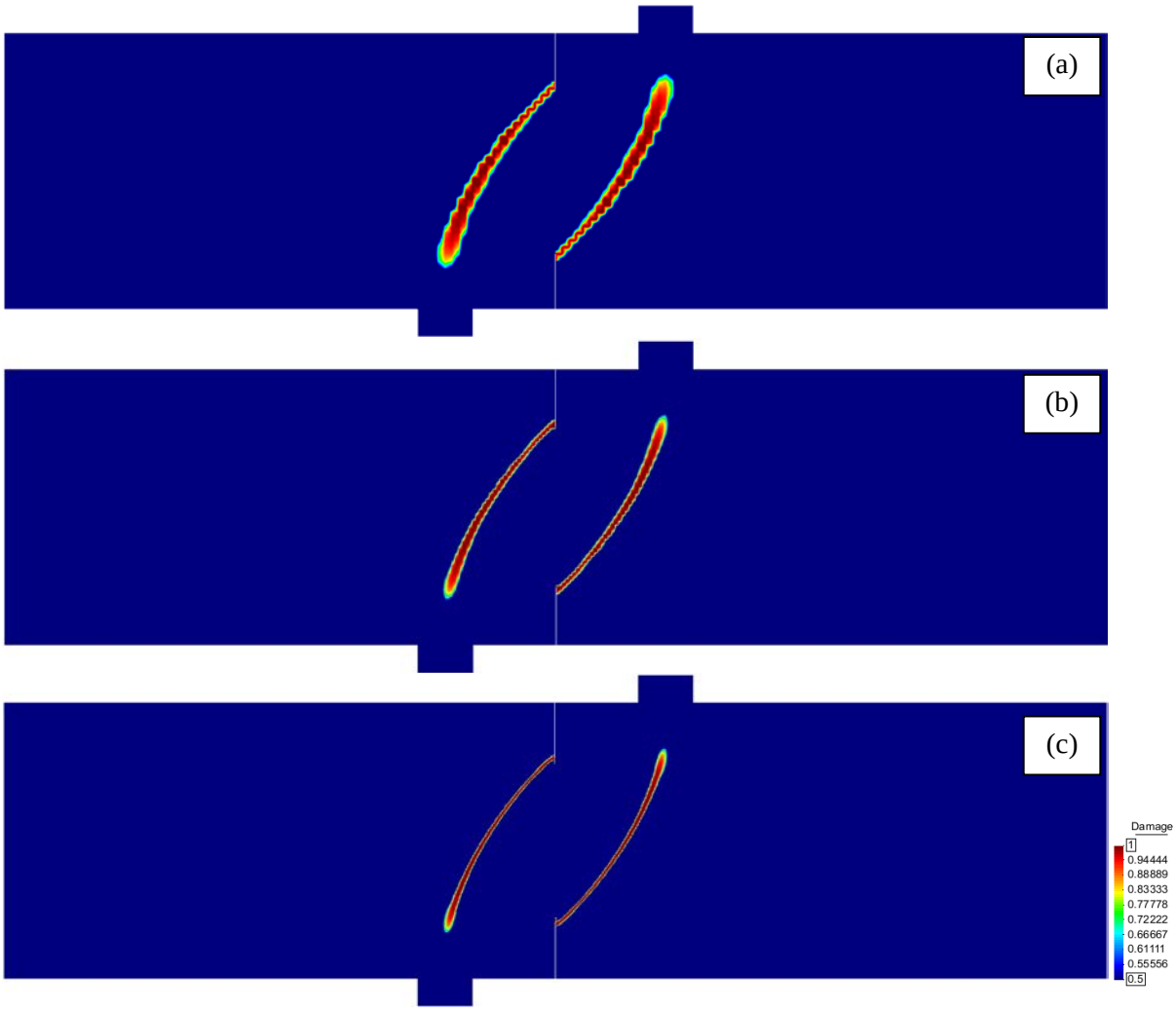

Figure 27. Damage contours of the Bocca beam with: (a) no AMR, (b) 1 level of AMR and (c) 2 levels of AMR

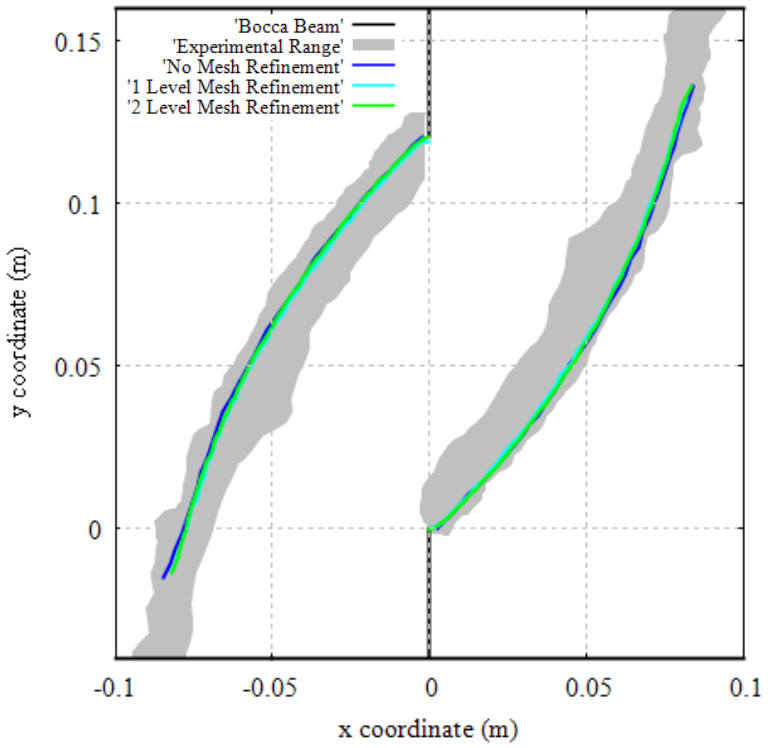

Figure 28. Detail of the computed crack trajectories for the different levels of mesh refinement of the Bocca beam

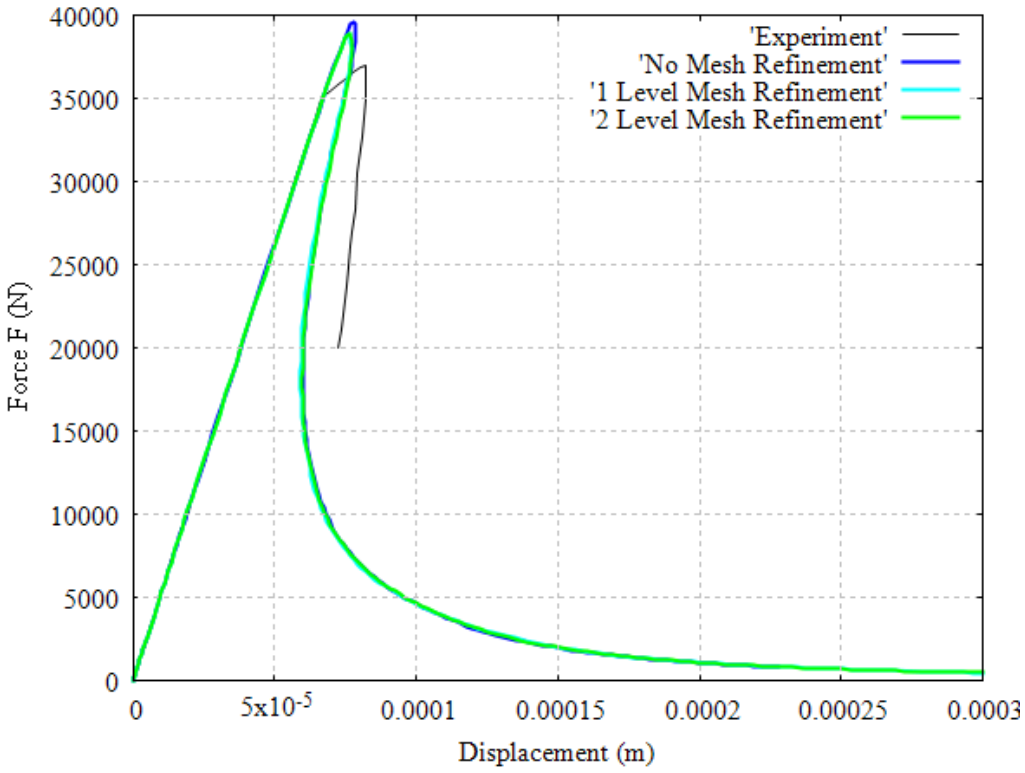

Figure 29. Computed force-displacement curves of the Bocca beam

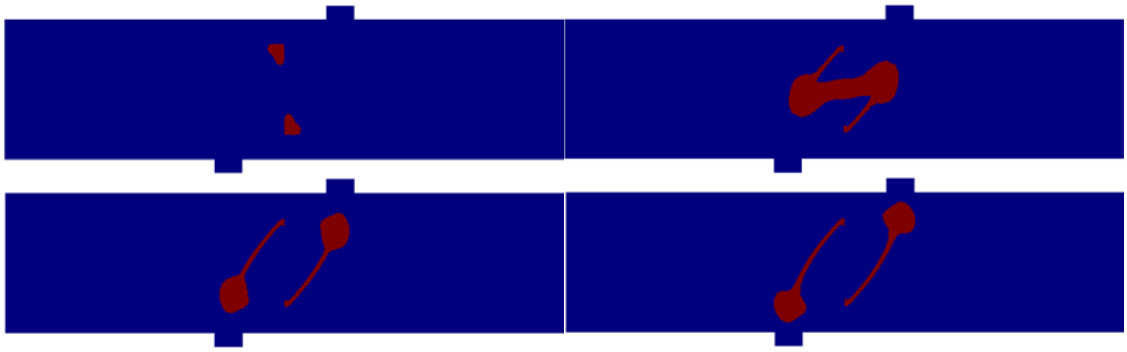

Figure 30. Evolution of the area where standard (in blue) and mixed (in red) formulations are adopted during the simulation with 2 level adaptive mesh refinement of the Bocca beam

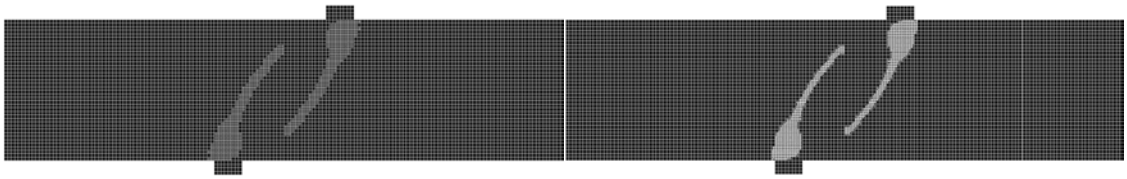

Figure 31. Meshes at the end of the simulations of the Bocca beam with (left) 1 level of AMR and (right) 2 levels of AMR

Figure 29 shows the results in terms of force F vs displacement curves at the upper right support. The three computations considered produce practically matching results, with a small overestimation of the bearing capacity in the case calculated with the coarse mesh. It can be observed how the simulations with 1 and 2 levels of AMR provide almost the same peak load. Figure 29 also details how the computed force-displacement curves agree with the experiment. This is remarkable, given that only one curve is provided for the original experiment in reference [55].

	Max. Ndofs standard FEs	Max. Ndofs mixed $\boldsymbol{\varepsilon/u}$ FEs	Max. Ndofs AFR	% of Ndofs with respect to mixed only	% of Ndofs with respect to standard only
Without AMR	13,378	40,134	17,230	42.93%	**128.79%**
1 level of AMR	21,878	65,634	29,894	45.55%	**136.64%**
2 levels of AMR	54,234	162,702	81,502	50.09%	**150.28%**

Table 8. Cost-efficiency of the proposed mesh and formulation adaptivity scheme for the Bocca beam

	Number of elements with initial uniform refinement	Max. number of elements with AMR	%
No mesh refinement	6,464	-	-
1 level of refinement	25,856	10,556	**40.83%**
2 levels of refinement	103,424	26,402	**25.53%**

Table 9. Cost-efficiency of the proposed mesh adaptivity scheme for the Bocca beam

In Figure 30 the evolution of the areas where standard and mixed FE formulations are active for different time-steps is shown. It can be seen how the proposed criterion defined in function of the equivalent effective stress is able of successfully delimiting the areas where mixed FEs should be activated in the considered case study where two different cracks are evolving. Figure

31 presents the meshes that result at the end of the simulation when the adaptive mesh refinement capabilities are introduced. It can be seen how the proposed model is also able to properly define the regions that required mesh refinement and later coarsening.

	CPU-times (s)		
	Standard FEs	AFR	Mixed FEs
Without AMR	757.09	1,193.07	5,248.93
1 level of AMR	4,091.41	4,390.56	18,556.28
2 levels of AMR	12,490.85	25,394.72	76,053.59

Table 10. CPU-times of the computations with standard FEs, mixed FEs and the proposed AFR scheme for the Bocca beam

In Table 8 the cost-efficiency of the proposed methodology is assessed. As in the previous cases, for each of the situations considered (without AMR, with 1 level of AMR and with 2 levels of AMR) the maximum number of degrees of freedom is indicated for analyzes performed with standard FE, mixed FE and AFR. The relation between the maximum number of degrees of freedom in AFR and the other two methods (standard only and mixed only) is also given. In the present analysis, where an initial coarse mesh is considered, it can be observed how the reduction in computational cost provided by AFR is not as important as in the previous sections where an initially fine mesh is adopted. Notwithstanding, the use of the AFR approach remains highly advantageous also in this instance.

Table 9 shows the cost-effectiveness of AMR in the Bocca beam analysis. For the three cases considered (without refinement, with 1 level of refinement and with 2 levels of refinement) the strategies of uniform refinement (first column) and adaptive refinement (second column) are compared in terms of the number of elements that ensue in the computation. In the third column the ratio between the two values is indicated. It can be observed how the AMR capabilities of the model provide a noteworthy reduction in computational cost.

To further show the increased efficiency ensuing from the adoption of the proposed AFR scheme, Table 10 compares the resulting CPU-times with corresponding simulations using standard and mixed FEs only. Again, each of the considered cases (without AMR, with 1 level of AMR and with 2 levels of AMR) are considered. Computations were carried out in a single thread on an Intel Core i7-6700 CPU. It can be observed that the CPU-times ensuing from the application of the AFR strategy are much lower the ones corresponding to the use of mixed FEs. The order of magnitude of the computational cost of AFR is comparable to the one resulting from the use of standard FEs. This shows that the AFR approach highly reduces the cost of the simulations performed with mixed FEs, while preserving the quality of the results.

4.4. Crack branching numerical test

In this section, the numerical simulation of a crack branching test is performed. In this benchmark, initially proposed in reference [62], a square plate with an initial notch at the midheight is considered in order to examine the ability of the numerical approach in reproducing bifurcations.

The geometry and boundary conditions of the problem are indicated in Figure 32a. The plate has dimensions of 2 mm x 2 mm. The thickness of the notch is taken as zero. The right edge of the plate is fixed and on the top and bottom boundaries are imposed vertical displacements following the function $f(x) = u_v(x-1)^2/4$, u_v being the displacement at the top-left and bottom-left corners and the origin $x = 0$ being placed at the center of the specimen so that $-1 \leq x \leq 1$. These imposed boundary conditions enforce the branching of the propagating crack in the plate. The material properties of the test are included in Table 11, used together with the Rankine damage surface.

The numerical simulation is performed with both AFR and AMR capabilities. In this case, 3 levels of mesh refinement are introduced. AMR is triggered when the equivalent effective stress $\bar{\sigma}_{eq}$ reaches 75% of the tensile strength f_t. Coarsening is enabled when $\bar{\sigma}_{eq}$ drops below 50% of f_t. The same thresholds are established for AFR.

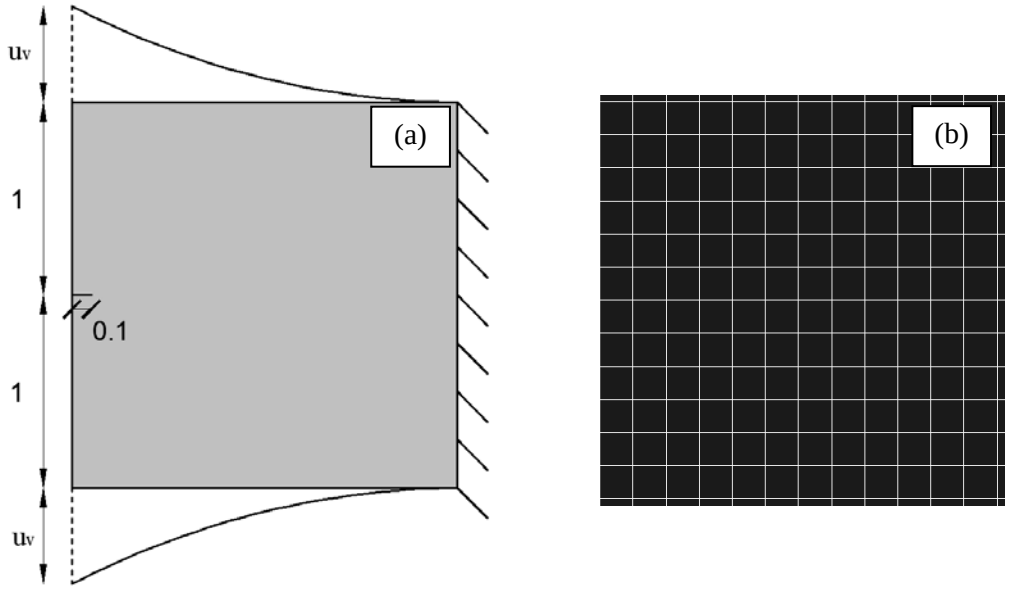

Figure 32. Crack branching numerical test: (a) Geometry (mm) and (b) detail of the mesh in the area of the notch

Young's Modulus	$20.0 \cdot 10^9$ Pa
Poisson's Ratio	0.3
Tensile Strength	$44.0 \cdot 10^6$ Pa
Tensile Fracture Energy	89 J/m^2

Table 11. Material properties of the crack branching numerical test

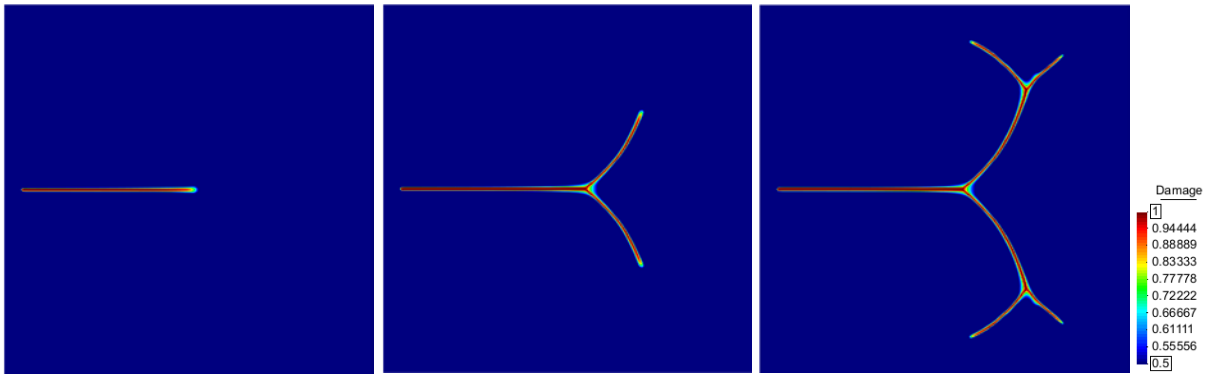

Figure 33. Computed damage contours at different stages of the simulation of the crack branching numerical test

The detail of the initial mesh adopted to perform the simulation in the area of the notch is shown in Figure 32b. It is a structured mesh of 40 x 40 = 1600 quadrilateral elements. Note that this original mesh is not fine enough to produce an acceptable result of the numerical simulation if AMR is not introduced. It has been chosen to illustrate the capabilities of the proposed numerical scheme when a coarse mesh is initially considered.

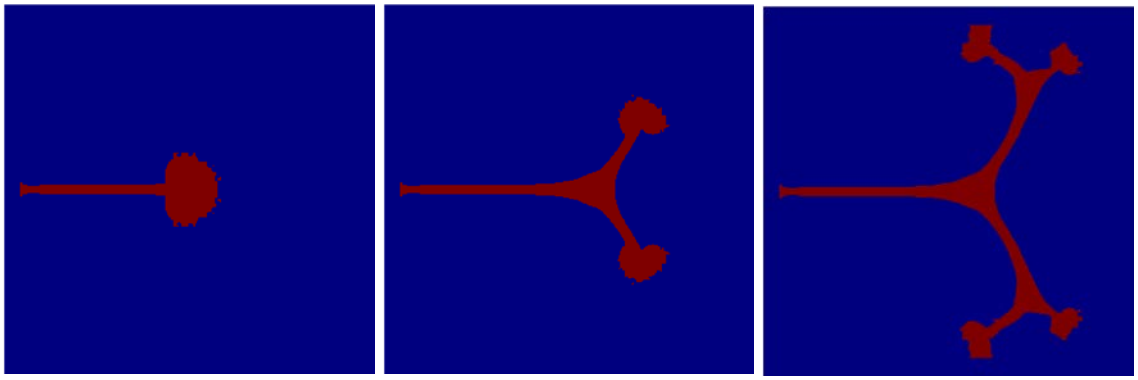

Figure 34. Crack branching numerical test: Evolution of the area where standard (in blue) and mixed (in red) formulations are adopted

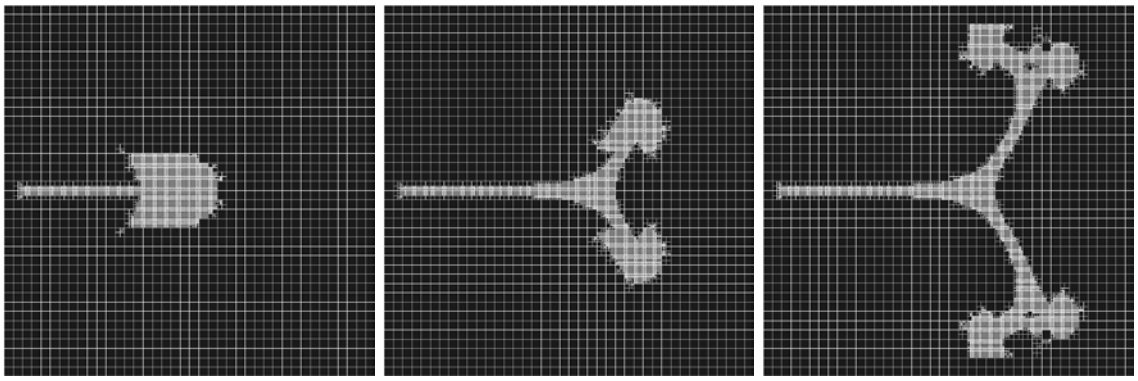

Figure 35. Crack branching numerical test: Evolution of the refined area

Max. Ndofs mixed $\boldsymbol{\varepsilon}/\boldsymbol{u}$ FEs	Max. Ndofs AFR	% of Ndofs with respect to mixed only
87,132	66,332	**76.13%**

Table 12. Cost-efficiency of the proposed formulation adaptivity scheme for the crack branching numerical test

Number of nodes with initial uniform refinement	Max. number of nodes with adaptive mesh refinement	%
103,057	14,522	**14.09**

Table 13. Cost-efficiency of the proposed mesh adaptivity scheme for the crack branching numerical test

In Figure 33 the computed damage contours at different stages of the simulation can be observed. It can be seen how first the crack progresses horizontally and then branches due to the boundary conditions imposed in the body. Two symmetric cracks evolve in the plate until branching occurs again. Then, four symmetric cracks propagate through the plate. Figure 34 shows the evolution of the area where the mixed FE formulation is activated during the simulation. It can be seen how mixed FEs are introduced in the simulation only in the areas where the cracks propagate. Also, in Figure 35 the regions where the mesh is refined can be observed for the same time steps. This shows that the proposed criterion based on the equivalent effective stress is satisfactorily defining the areas to be refined in crack branching situations as well.

Table 12 assesses the savings in computational cost due to the proposed AFR scheme. The first column indicates the maximum number of degrees of freedom (labelled Max. Ndofs) ensuing from computations with mixed FE only while the second column shows the corresponding value for the AFR strategy. The last column presents the relation between the two previous values. In the present case where an initial coarse mesh is adopted, the decrease in the number of degrees of freedom is due to the AFR scheme is not as important as in the previous case study where an initially fine mesh was employed. Still, the FE formulation adaptivity allows to introduce a significant reduction in computational cost.

Table 13 examines the cost-efficiency of the adopted AMR strategy. In the first column the number of nodes resulting from the use of an initial uniform refinement approach is provided while in the second column the number of nodes introduced by the ARM method is indicated. The third column shows the relation between the two previous values. It can be inferred that in this case where an initial coarse mesh is adopted to calculate the problem, AMR produces a large saving in the computational cost with respect to the use of initial mesh refinement.

In the present case study, the adaptive mesh refinement strategy produces a large part of the total cost savings of the method. No sign of spurious mesh bias dependence can be observed. The combination of the AMR and AFR capabilities of the proposed model allows to obtain mesh objective results at a reasonable computational cost.

5. Conclusions

In this work, the use of an Adaptive Formulation Refinement (AFR) strategy is combined with the application of an Adaptive Mesh Refinement (AMR) approach for the cost-efficient computation of localized structural failure with enhanced accuracy and mesh objectivity.

The proposed AFR strategy allows to adaptively switch between the standard displacement-based FE formulation and the more accurate mixed strain/displacement FE. An isotropic damage model is used to model the stiffness degradation leading to cracking and structural failure. A simple and effective criterion defined in terms of the ratio between the equivalent effective stresses that develop in the structure and the material strength is introduced to selectively activate the formulations. The proposed methodology has shown to significantly reduce the computational cost of the simulations, rendering them of the order of standard FE calculations, while benefitting from the enhanced accuracy and mesh bias objectivity of the mixed FE.

Using a similar refinement criterion based on the same ratio between the equivalent effective stresses and the material strength, the adopted AMR strategy further reduces the required computational cost of structural analyses, by allowing to start the simulation with a coarse mesh and adaptively refining only the areas where crack propagation occurs, which represent a small part of the whole domain.

The proposed model also allows for the later adaptive mesh coarsening and *formulation derefinement*, switching back from mixed to standard FEs, according to the corresponding criteria. The combination of the AFR and AMR methodologies is fairly straightforward.

The paper includes the assessment of the proposed methodology through the simulation of several numerical benchmarks and experimental tests available in the literature. The successful computation of situations involving structural size effect, multiple developing cracks and crack branching is presented. The simulations reproduce the bearing capacity, force-displacement curves, crack trajectories and collapse mechanism observed in the experiments with enhanced accuracy.

Complementarily, the comparison of the proposed model with the standard displacement-based formulation is also performed. This shows, on the one hand, the capacity of the adopted methodology combining AFR and AMR to produce converging mesh objective results, without any trace of spurious mesh dependence. On the other hand, the standard formulation alone remains spuriously mesh dependent and unreliable, even if the mesh is refined.

Calculations show the capacity of the approach integrating AFR and AMR to obtain reliable results with high accuracy and with a computational cost of the order of the standard displacement-based FE. This demonstrates the effectiveness of the approach in engineering practice.

6. Acknowledgements

Financial support from the European Union's horizon 2020 research and innovation programme (H2020-DT-2019-1 No. 872570) under the KYKLOS 4.0 Project (An Advanced Circular and Agile Manufacturing Ecosystem based on rapid reconfigurable manufacturing process and individualized consumer preferences) and by the Spanish Ministry of Science, Innovation and Universities via the Primus project (Computational Framework for Additive Manufacturing of Titanium Alloy) project (Printing pattern based and MultiScale enhanced performance analysis of advanced Additive Manufacturing components, ref. num. PID2020-115575RB-I00) is gratefully acknowledged. The authors also acknowledge financial support from the Spanish Ministry of Economy and Competitiveness, through the "Severo Ochoa Programme for Centres of Excellence in R&D" (CEX2018-000797-S).

7. References

[1] J. Rots, P. Nauta, G. Kusters and J. Blauwendraad, "Smeared crack approach and fracture localization in concrete," *Heron,* vol. 30, pp. 1-48, 1985.

[2] J. Rots, "Computational modeling of concrete fracture," *Ph.D. Thesis, Delft University of Technology,* 1988.

[3] J. Oliver, M. Cervera, S. Oller and J. Lubliner, "Isotropic damage models and smeared crack analysis of concrete," *II Int. conference on computer aided analysis and design of concrete,* pp. 945-957, 1990.

[4] L. Sluys, "Wave propagation localisation and dispersion in softening solids," *Ph.D. Thesis, Delft University of Technology,* 1992.

[5] T. Rabczuk, "Computational methods for fracture in brittle and quasi-brittle solids: State-of-the-art review and future perspectives," *ISRN Applied Mathematics,* vol. 2013, p. 849231, 2013.

[6] M. Cervera, G. Barbat, M. Chiumenti and J.-Y. Wu, "A Comparative Review of XFEM, Mixed FEM and Phase-Field Models for Quasi-brittle Cracking," *Archives of Computational Methods in Engineering,* vol. 29, pp. 1009-1083, 2022.

[7] M. Cervera, M. Chiumenti and R. Codina, "Mixed stabilized finite element methods in nonlinear solid mechanics. Part I: Formulation," *Computer Methods in Applied Mechanics and Engineering,* vol. 199, no. 37-40, pp. 2559-2570, 2010.

[8] M. Cervera, M. Chiumenti and R. Codina, "Mixed stabilized finite element methods in

nonlinear solid mechanics. Part II: Strain localization," *Computer Methods in Applied Mechanics and Engineering,* vol. 199, no. 37-40, pp. 2571-2589, 2010.

[9] M. Cervera and M. Chiumenti, "Smeared crack approach: back to the original track," *International Journal for Numerical and Analytical Methods in Geomechanics,* vol. 30, no. 12, pp. 1173-1199, 2006.

[10] M. Cervera, M. Chiumenti and R. Codina, "Mesh objective modeling of cracks using continuous linear strain and displacement interpolations," *International Journal for Numerical Methods in Engineering,* vol. 87, no. 10, pp. 962-987, 2011.

[11] M. Cervera, G. Barbat and M. Chiumenti, "Finite element modelling of quasi-brittle cracks in 2D and 3D with enhanced strain accuracy," *Computational Mechanics,* vol. 60, no. 5, pp. 767-796, 2017.

[12] G. Barbat, M. Cervera and M. Chiumenti, "Appraisement of planar, bending and twisting cracks in 3D with isotropic and orthotropic damage models," *International Journal of Fracture,* vol. 210, no. 1-2, pp. 45-79, 2018.

[13] G. Vlachakis, M. Cervera, G. Barbat and S. Saloustros, "Out-of-plane seismic response and faillure mechanism of masonry structures using finite elements with enhanced strain accuracy," *Engineering Faillure Analysis,* vol. 97, pp. 534-555, 2019.

[14] M. Cervera, G. Barbat and M. Chiumenti, "Architecture of a multi-crack model with full closing, reopening and sliding capabilities," *Computational Mechanics,* vol. 65, no. 6, pp. 1593-1620, 2020.

[15] G. Barbat, M. Cervera, M. Chiumenti and E. Espinoza, "Structural size effect: experimental, theoretical and accurate computational assessment," *Engineering Structures,* vol. 213, p. 110555, 2020.

[16] C. Agelet de Saracibar, M. Chiumenti, Q. Valverde and M. Cervera, "On the orthogonal subgrid scale pressure stabilization of finite deformation J2 plasticity," *Computer Methods in Applied Mechanics and Engineering,* vol. 195, no. 9-12, pp. 1224-1251, 2006.

[17] M. Chiumenti, M. Cervera and R. Codina, "A mixed three-field FE formulation for stress accurate analysis including the incompressible limit," *Computer Methods in Applied Mechanics and Engineering,* vol. 283, pp. 1095-1116, 2015.

[18] M. Chiumenti, M. Cervera, C. Moreira and G. Barbat, "Stress, strain and dissipation accurate 3-field formulation for inelastic isochoric deformation," *Finite Elements in Analysis and Design,* vol. 192, p. 103534, 2021.

[19] C. Moreira, G. Barbat, M. Cervera and M. Chiumenti, "Accurate thermal-induced structural failure analysis under incompressible conditions," *Engineering Structures,* vol. 261, p. 114213, 2022.

[20] H. Venghaus, M. Chiumenti, J. Baiges, D. Juhre and I. Castañar, "An accurate approach to simulate the friction stir welding process using adaptive formulation refinement," *in preparation,* 2022.

[21] M. Borden, C. Verhoosel, M. Scott, T. Hughes and C. Landis, "A phase-field description of dynamic brittle fracture," *Computer Methods in Applied Mechanics and Engineering,* Vols.

217-220, pp. 77-95, 2012.

[22] T. Heister, M. Wheeler and T. Wick, "A primal-dual active set method and predictor-corrector mesh adaptivity for computing fracture propagation using a phase-field approach," *Computer Methods in Applied Mechanics and Engineering,* vol. 290, pp. 466-495, 2015.

[23] S. Zhou and X. Zhuang, "Adaptive phase field simulation of quasi-static crack propagation in rocks," *Underground Space,* vol. 3, no. 3, pp. 190-205, 2018.

[24] N. Ferro, S. Micheletti and S. Perotto, "Anisotropic mesh adaptation for crack propagation induced by a thermal shock in 2D," *Computer Methods in Applied Mechanics and Engineering,* vol. 331, pp. 138-158, 2018.

[25] Hirshikesh, C. Jansari, K. Kannan, R. Annabattula and S. Natarajan, "Adaptive phase field method for quasi-static brittle fracture using a recovery based error indicator and quadtree decomposition," *Engineering Fracture Mechanics,* vol. 220, p. 106599, 2019.

[26] J. Baiges and C. Bayona, "Refficientlib: An efficient load-rebalanced adaptive mesh refinement algorithm for high-performance computational physics meshes," *SIAM Journal on Scientific Computing,* vol. 39, no. 2, pp. 65-95, 2017.

[27] J. Baiges, R. Codina, A. Pont and E. Castillo, "An adaptive fixed-mesh ALE method for free surface flows," *Computer Methods in Applied Mechanics and Engineering,* vol. 313, pp. 159-188, 2017.

[28] J. Baiges, M. Chiumenti, C. Moreira, M. Cervera and R. Codina, "An adaptive finite element strategy for the numerical simulation of additive manufacturing processes," *Additive Manufacturing,* vol. 37, p. 101650, 2021.

[29] C. Moreira, M. Caicedo, M. Cervera, M. Chiumenti and J. Baiges, "A multi-criteria h-adaptive finite element framework for industrial part-scale thermal analysis in additive manufacturing processes," *Engineering with Computers,* 2022.

[30] Y. Rashid, "Ultimate strength analysis of prestressed concrete pressure vessels," *Nuclear Engineering and Design,* vol. 7, no. 4, pp. 334-344, 1968.

[31] Z. Bazant and B. Oh, "Crack band theory for fracture of concrete," *Matériaux et Constructions,* vol. 16, no. 3, pp. 155-177, 1983.

[32] J.-Y. Wu, J.-F. Qiu, V. Nguyen, T. Mandal and L.-J. Zhuang, "Computational modeling of localized failure in solids: XFEM vs PF-CZM," *Computer Methods in Applied Mechanics and Engineering,* vol. 345, pp. 618-643, 2019.

[33] M. Cervera, M. Chiumenti, L. Benedetti and R. Codina, "Mixed stabilized finite element methods in nonlinear solid mechanics. Part III: Compressible and incompressible plasticity," *Computer Methods in Applied Mechanics and Engineering,* vol. 285, no. 0, pp. 752-775, 2015.

[34] L. Benedetti, M. Cervera and M. Chiumenti, "3D modelling of twisting cracks under bending and torsion skew notched beams," *Engineering Fracture Mechanics,* vol. 176, pp. 235-256, 2017.

[35] S. Saloustros, M. Cervera, S. Kim and M. Chiumenti, "Accurate and locking-free analysis of beams, plates and shells using solid elements," *Computational Mechanics,* vol. 67, pp. 883-914, 2021.

[36] F. Brezzi and K. Bathe, "A Discourse on the Stability Conditions for Mixed Finite Element Formulations," *Computer Methods in Applied Mechanics and Engineering,* vol. 82, pp. 27-59, 1990.

[37] F. Brezzi, "On the existence, uniqueness and approximation of saddle-point problems arising from lagrangian multipliers," *ESAIM: Mathematical Modelling and Numerical Analysis - Modélisation Mathématique et Analyse Numérique,* vol. 8, no. R2, pp. 129-151, 1974.

[38] F. Brezzi and M. Fortin, Mixed and Hybrid Finite Element Methods, New York: Springer, 1991.

[39] I. Babuska, "Error-bounds for finite element method," *Numerisch Mathematik,* vol. 16, pp. 322-333, 1971.

[40] D. Boffi, F. Brezzi and M. Fortin, "Mixed Finite Element Methods and Applications," *Springer,* 2013.

[41] R. Codina, "Stabilization of incompressibility and convection through orthogonal sub-scales in finite element methods," *Computer Methods in Applied Mechanics and Engineering ,* vol. 190, pp. 1579-1599, 2000.

[42] T. Hughes, "Multiscale phenomena: Green's function, Dirichlet-to-Neumann formulation, subgrid scale models, bubbles and the origins of stabilized formulations," *Computer Methods in Applied Mechanics and Engineering,* vol. 127, no. 1-4, pp. 387-401, 1995.

[43] R. Codina, "Analysis of a stabilized finite element approximation of the Oseen equations using orthogonal subscales," *Applied Numerical Mathematics,* vol. 58, pp. 264-283, 2008.

[44] R. Codina, "Finite element approximation of the three field formulation of the Stokes problem using arbitrary interpolations," *Society for Industrial and Applied Mathematics Journal on Numerical Analysis,* vol. 47, pp. 699-718, 2009.

[45] S. Badia and R. Codina, "Unified stabilized finite element formulations for the Stokes and the Darcy problems," *SIAM Journal on Numerical Analysis,* vol. 17, pp. 309-330, 2009.

[46] L. Benedetti, M. Cervera and M. Chiumenti, "High-fidelity prediction of crack formation in 2D and 3D pullout tests," *Computers and Structures,* vol. 172, pp. 93-109, 2016.

[47] L. Benedetti, M. Cervera and M. Chiumenti, "Stress-accurate mixed FEM for soil failure under shallow foundations involving strain localization in plasticity," *Computers and Geotechnics,* vol. 64, pp. 32-47, 2015.

[48] M. Cervera, J.-Y. Wu, M. Chiumenti and S. Kim, "Strain localization analysis of Hill's orthotropic elastoplasticity: Analytical results and numerical verification," *Computational Mechanics,* vol. 65, pp. 533-554, 2019.

[49] L. Benedetti, Mixed finite element formulations for strain localization and failure in plasticity, Ph.D. Thesis, Technical University of Catalonia, 2017.

[50] A. Coll, R. Ribo, M. Pasenau, E. Escolano, J. S. Perez, A. Melendo, A. Monros and J. Garate, "GiD: the personal pre and post-processor User Manual," *CIMNE, Technical University of Catalonia,* p. <http://gid.cimne.upc.edu>, 2002.

[51] V. Garcia-Alvarez, R. Gettu and I. Carol, "Analysis of mixed-mode fracture in concrete using interface elements and a cohesive crack model," *Sadhana,* vol. 37, no. 1, pp. 187-205, 2012.

[52] D.-C. Feng and J.-Y. Wu, "Phase-field regularized cohesive zone model (CZM) and size effect of concrete," *Engineering Fracture Mechanics,* vol. 197, pp. 66-79, 2018.

[53] G. Barbat, Mixed finite elements with independent strain interpolation for isotropic and orthotropic damage, Ph.D. Thesis, Technical University of Catalonia, 2021.

[54] M. Arrea and A. Ingraffea, "Mixed-mode crack propagation in mortar and concrete," Tech. Rep. Report No. 81-13, Department of Structural Engineering, Cornell University, New York, 1982.

[55] P. Bocca, A. Carpinteri and S. Valente, "Mixed mode fracture of concrete," *International Journal of Solids and Structures,* vol. 27, no. 9, pp. 1139-1153, 1991.

[56] T. Rabczuk and T. Belytschko, "Cracking particles: a simplified meshfree method for arbitrary evolving cracks," *International Journal for Numerical Methods in Engineering,* vol. 61, pp. 2316-2343, 2004.

[57] T. Rabczuk and G. Zi, "A meshfree method based on the local partition of unity for cohesive cracks," *Computational Mechanics,* vol. 39, pp. 743-760, 2006.

[58] A. Saleh and M. Aliabadi, "Crack growth analysis in concrete using boundary element method," *Engineering Fracture Mechanics,* vol. 51, no. 4, pp. 533-545, 1995.

[59] Y. Zhang, R. Lackner, M. Zeiml and H. Mang, "Strong discontinuity embedded approach with standard SOS formulation: element formulation, energy-based crack-tracking strategy, and validations," *Computer Methods in Applied Mechanics and Engineering,* vol. 287, pp. 335-366, 2015.

[60] P. Areias, T. Rabczuk and D. Dias-da-Costa, "Element-wise fracture algorithm based on rotation of edges," *Engineering Fracture Mechanics,* vol. 110, pp. 113-137, 2013.

[61] P. Areias, T. Rabczuk and J. Cesar de Sa, "A novel two-stage discrete crack method based on the screened Poisson equation and local mesh refinement," *Computational Mechanics,* vol. 58, pp. 1003-1018, 2016.

[62] A. Muixi, O. Marco, A. Rodriguez-Ferran and S. Fernandez-Mendez, "A combined XFEM phase-field computational model for crack growth without remeshing," *Computational Mechanics,* vol. 67, pp. 231-249, 2021.